Short-Term Wind Power Forecasts using Doppler Lidar
by
Beth Magerman

A Thesis Presented in Partial Fulfillment
of the Requirements for the Degree
Master of Science

Approved November 2014 by the
Graduate Supervisory Committee:

Ronald Calhoun, Chair
Yulia Peet
Huei-Ping Huang
Raghavendra Krishnamurthy

ARIZONA STATE UNIVERSITY

December 2014

ABSTRACT

With a ground-based Doppler lidar on the upwind side of a wind farm in the Tehachapi Pass of California, radial wind velocity measurements were collected for repeating sector sweeps, scanning up to 10 kilometers away. This region consisted of complex terrain, with the scans made between mountains. The dataset was utilized for techniques being studied for short-term forecasting of wind power by correlating changes in energy content and of turbulence intensity by tracking spatial variance, in the wind ahead of a wind farm. A ramp event was also captured and its propagation was tracked.

Orthogonal horizontal wind vectors were retrieved from the radial velocity using a sector Velocity Azimuth Display method. Streamlines were plotted to determine the potential sites for a correlation of upstream wind speed with wind speed at downstream locations near the wind farm. A “virtual wind turbine” was “placed” in locations along the streamline by using the time-series velocity data at the location as the input to a modeled wind turbine, to determine the extractable energy content at that location. The relationship between this time-dependent energy content upstream and near the wind farm was studied. By correlating the energy content with each upstream location based on a time shift estimated according to advection at the mean wind speed, several fits were evaluated. A prediction of the downstream energy content was produced by shifting the power output in time and applying the best-fit function. This method made predictions of the power near the wind farm several minutes in advance. Predictions were also made up to an hour in advance for a large ramp event. The Magnitude Absolute Error and Standard Deviation are presented for the predictions based on each selected upstream location.

DEDICATION

I dedicate this work to my dad, Leonard, who always believed in me and would have been so proud to see me complete a Master's degree and follow in his footsteps as a mechanical engineer. I have enormous appreciation for everyone who supported and encouraged me during this process, especially my mom, Irene, and my sister, Hayley, who always believe in me, my boyfriend who was incredible at helping me stay focused and not become too stressed, and my friends who were always there when I needed a break.

ACKNOWLEDGMENTS

I would like to thank Dr. Ronald Calhoun for advising me in this project. I would also like to express appreciation to the entire ASU Environmental Remote Sensing research team, including Nihanth Cherukuru, Trent Hoffman, Kai Zhou, Sree Bhuskaran, Lara Thurman, and graduated student Aditya Choukulkar, who are always supportive and collaborative. I would also like to thank Chris Bremer for suggestions on computational mathematics. I want to thank ASU's Graduate Writing Center for their assistance in the writing process. We would like to thank Beyond Photonics and Lockheed Martin Coherent Technologies for support of our equipment.

We have a great deal of gratitude to Bjorn Doskeland and Eric Krajeski of Windland, Inc. for accommodating our lidar and experimental work on their wind farm in Tehachapi, California.

We recognize the support of the Electric Power Research Institute (EPRI), sponsor award 10001389 (Program Officer: Dr. Aidan Tuohy) which made this work possible. We would also like to thank Jim Blatchford of CA ISO for his support.

Special thanks to Dr. Raghuvendra Krishnamurthy for his comments and contributions as well as Dr. Yulia Peet and Dr. Huei-Ping Huang for their valuable input.

TABLE OF CONTENTS

Page

CHAPTER Page

LIST OF TABLES

Table Page

LIST OF FIGURES

Figure Page

Figure Page

Figure Page

Figure Page

Figure Page

Chapter 1

INTRODUCTION

As wind power becomes a more substantial component of the electrical grid, its intermittency causes unreliability in the grid that requires additional forecasting capability to mitigate (Lange & Focken, 2006, p. 3). Wind farm generation provided to the grid is scheduled conservatively to avoid underperformance, and sudden changes in power output, called ramp events, decrease stability of the grid and must be balanced by other power sources (Parks, Wan, Wiener, & Liu, 2011). Turbulent winds cause high loading on wind turbines which decreases the lifespan of the turbines (Frehlich, 2013). Advanced knowledge of changes in wind power make it possible for wind farm operators to modify their control systems to improve their reliability, capture more power, and decrease the loading on turbines when scheduled electrical demand is lower than the available wind power (Zhang, Wang, & Wang, 2014).

Wind power is extracted from kinetic energy in the wind by placing a turbine into the wind stream. The wind exerts lift and drag onto the turbine blades, rotating the turbine. Modern wind turbines usually operate at variable, low speeds, between 30 and 60 revolutions per minute, controlled by changing the pitch of the blades. The rotating turbine turns a shaft that provides an input to a gearbox which increases the angular velocity. The rotating shaft leaving the gearbox transmits the torque to a generator that converts the rotational kinetic energy to electricity, which is transmitted to a transformer and supplied to the electrical grid.

Since the wind power is dependent on the wind speed, unforeseen changes in the atmospheric conditions cause unanticipated variations in the power output of the wind turbine. As a result, observations of meteorological conditions and predictions of variation in the wind provide useful information to wind farm operators (Lange & Focken, 2006). Short term predictions inform operators of impending fluctuations in the wind farm output, such that they can make operations decisions to best meet their requirements. Measurements were made in the 'upstream' direction for the current experiment ("NOAA's National Weather Service," n.d.). Upstream is defined as "towards the source of flow, or located in the area from which the flow is coming." The method being applied uses real-time measurements of wind velocity taken upstream of the wind farm and models the power output of a turbine as though it were located upstream. A modifying function is applied based on correlation studies of the relationship between measurements made at the upstream location and near the actual wind farm, to predict the extractable power available in the oncoming wind. Regions of high turbulent intensity in this oncoming wind are predicted from the spatial variance of the wind speed, the difference between the speed advecting toward the wind farm and the average speed measured over a given distance downstream, closer to the wind farm. Ramp events propagating from directions other than upstream are studied by comparison of the profiles at locations across the scan domain to track and monitor large changes in the extractable power. The ramp events can also be detected visually in radial velocity plots when a region of higher magnitude is seen moving through the scan domain in successive plots.

Chapter 2

THEORETICAL BACKGROUND

Wind is created when pressure differences over parts of the earth's surface occur since air masses to move from places of high pressure to places of low pressure (Brower, 2012, p. 2-4). The continual diurnal solar heating of the earth's surface creates surface temperature differences. Over hot surfaces, the air is heated, which results in expansion and rising of the air and a decrease in pressure. Surface cooling causes the opposite process, causing an increase in pressure. This pressure difference due to the earth's uneven solar heating is the wind's driving force. Other effects, such as the Coriolis effect due to the rotational reference frame of the earth's surface, also contribute to the air movement experienced in the atmosphere.

A sea breeze is a mesoscale circulation caused by pressure differences in coastal regions (Brower, 2012, p. 2-4). Sea breezes become strong where they are concentrated by the terrain and are the primary mechanism driving strong winds in coastal mountain passes in places such as California. Sea breezes occur because, during a typical summer day, the land becomes warmer than the ocean. The warmer air over the land expands and rises, causing the pressure to drop, so that the relatively cool, dense air over the ocean is pulled in. A land breeze occurs at night when the process happens in reverse. The topography of the region and the density of the air mass both impact the movement of the air. Wind typically accelerates over rises in the terrain, such as ridges that are oriented transverse to the flow, but the dense air of a sea breeze often is forced instead to move through mountain passes as it is heavy compared to the surrounding air.

Figure 1 depicts the stratified layers within the troposphere (Lange & Focken, 2006, p. 24). Winds within the surface layer are affected by the surface of the earth, losing momentum due to drag from the surface. A typical vertical wind profile is shown, consisting of a logarithmic increase in wind speed with height above ground level. Wind turbines are located within the surface layer, often with hub heights up to 80 meters above ground level.

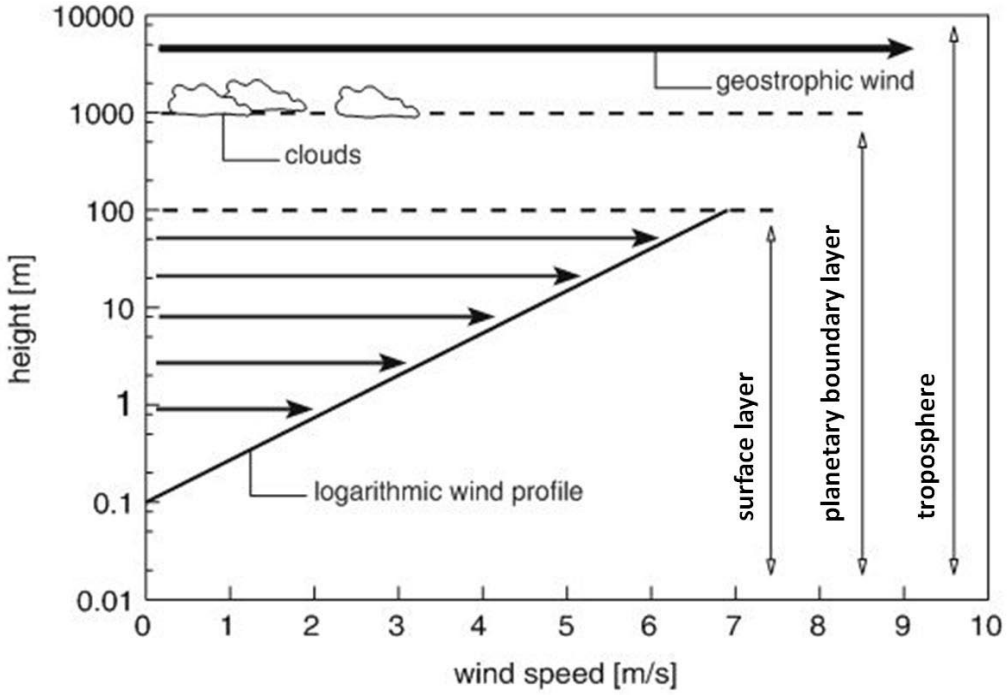

Figure 1. Layers of the Troposphere (Lange & Focken, 2006, p. 24). Reproduced with kind permission of Springer Science+Business Media © Springer 2006.

2.1 Remote Sensing

The measurements for this study are made through remote sensing. By using remote sensing, it is possible to make measurements over a large space much more quickly than *in situ* measurements, for which the measurement device must be situated at

the location of interest. The remote sensing device can be located in one place and make measurements of conditions in the surrounding area using properties of radiation. Active remote sensing can be done by emitting radiation at certain wavelengths and measuring the backscatter radiation. While radar, using radio waves, can only make atmospheric measurements from precipitation and visible clouds, it is possible to make measurements of naturally occurring aerosol particles in clear air by using light waves (Hutton, 2008).

To determine wind speed, the shift in frequency of the radiation is measured. Called the Doppler frequency shift, this frequency shift occurs when radiation is reflected from a particle moving along the direction of travel of the emitted radiation, referred to as the line of sight, and is related to the instantaneous speed of the particle along this direction. The Doppler frequency shift, $\Delta\nu$, is

$$\Delta\nu = -{}^{2v_r}/_{\lambda} \tag{1}$$

where v_r is the radial velocity, and λ is the operating wavelength (Hutton, 2008). Algorithms work in conjunction with the remote sensing devices to interpret the frequency shift by evaluating the frequency spectrum of the reflected radiation in order to determine the velocity of the particle along the line of sight direction.

It is assumed that the particles are suspended and have low enough slip with the surrounding air flow that their measured speed is representative of the speed of the air in the particles' vicinity. There is great flexibility in the acquisition method for remote measurement technologies. Remote sensing devices can make remote measurements from the ground, from airplanes, and from satellites.

This study employed a Windtracer lidar to measure wind speeds along its line of sight at up to 10 kilometers from its location. Named for the acronym of Light Detection and Ranging and also referred to as an infrared Doppler radar, the lidar is an active remote sensing instrument that emits an eye-safe, infrared beam and measures the backscatter from the atmospheric particles to calculate the Doppler Frequency Shift. This lidar emits a coherent beam with a wavelength of 1.6 μm, with very little divergence such that side lobe reflection is eliminated and that the sampling volume is not substantially changed even at far ranges (Hutton, 2008). A laser local oscillator is used for the heterodyne, or coherent, detection for very high sensitivity (Hutton, 2008). The light beam is transmitted in pulses with a length of approximately 90 meters and at a rate of 500 pulses per second, or a pulse repetition frequency (PRF) of 500 Hertz (Hutton, 2008). According to the distance from the lidar, the beams are 10-30 centimeters wide (Hutton, 2008). Two typical types of scan methods are made using a lidar, PPI (Plan Position Indicator- only varying azimuth) or RHI (Range Height Indicator- only varying elevation) (Hutton, 2008). Further details about the Windtracer lidar system are provided in Table 1.

Table 1. Summary of System Functionality, adapted from Lockheed Martin Coherent Technologies (Hutton, 2008).

Mode	Performance	Comments
Base Wind and Aerosol Profiling	Max Range: 10km (atmos. condition dependent) Range Resolution: 50 - 100 m Minimum Range: 400 m Accuracy: 0.5-1 m/sec, range dependent Line of Sight Update Rate: 0.1-20 Hz Spatial Res: 100x100m to 200x400m typical Max Height: 2-4 km	Range-resolved radial velocity, SNR and spectral width; System scanning in azimuth at fixed elevation angle (PPI) and or in elevation at fixed azimuth angle (PPI)

The remote sensing capability of the lidar provides measurements that can cover a wider area in a shorter time than would be possible with *in situ* measurements by balloon sounders or aircraft sounders, better representing the small-scale changes in wind speed throughout the atmosphere.

2.2 Literature Review

2.2.1 Wind Forecasting

Zhang et al. (2014) created a breakdown of the applicability of different time-ahead forecasts for the wind power industry. The current study examines a method of very short-term forecasting on the order of ten minutes. According to Zhang et al., the forecast of wind at this time horizon provides operators with information that contributes to control of the wind farm and to power system frequency control which improves reliability on the grid. Also examined in the current research are detection and advance

notification of ramp events on the order of an hour. Projections on this time-scale contribute to improved electrical grid scheduling of power sources and reserve requirements (Zhang et al.) to optimize power capture and ensure wind power decreases are balanced.

Krishnamurthy (2013) studied how lidar measurements can represent the wind field and how predictions of the wind at the wind farm can be used as an input for control methods to meet the needs of wind farm operators. The current work uses the lidar measurements and a correlation to make the control system input more closely represent the actual wind that will be experienced at the wind farm.

An understanding of the limitations of current wind forecasting methods, particularly in monitoring sudden large changes in wind power, called ramps, and the existing efforts related to upstream measurements to make wind power and turbulence predictions using correlation methods provides a context for this study.

A study produced by National Renewable Energy Laboratory (NREL) on a wind power forecasting collaboration between the National Center for Atmospheric Research (NCAR) and Xcel Energy, a company that manages wind power generation as well as fossil, nuclear, and hydro based generation, was performed to make improvements to wind power forecasting to improve the efficiency and reliability of wind power grid integration (Parks et. al, 2011). The paper notes that for common wind forecast models used at wind farms, significant ramp events are often poorly predicted or not predicted at all as a result of imprecision in the meteorological conditions modeled (Parks et. al, 2011, p. 2). Weather models may capture large-scale ramps, such as cold fronts, but often

incorrectly predict their time of arrival by minutes to hours. Weather models often miss smaller scale events, for example outflows due to convective activity. The limited ability of the forecasts in making predictions of the magnitude and timing of ramp events cause grid operators to schedule wind power output conservatively to avoid having to balance unexpected changes in power. The report details the method NCAR uses for improving the forecasting used by Xcel Energy (Parks et. al, 2011, p. 24). They apply a mesoscale ensemble prediction model which gives a probabilistic wind prediction through numerical weather prediction (NWP) modeling as the core forecasting system. This model has skill predicting power ramps from large-scale weather events, but needs improvement for predicting the time, magnitude, and duration of intermediate and smaller-scale events. To meet the need for short-term ramp forecasting, Doppler radar and public meteorological data near the wind farm are added. The reflectivity and radial velocity measured by the Doppler radar are assimilated into a numerical model and correctly detected oncoming ramps in preliminary tests, suggesting the Doppler radar is useful for providing warnings of ramp events on the scale of 0-2 hours.

From Frehlich's study, 'Scanning Doppler Lidar for Input into Short-Term Wind Power Forecasts' (2013), it was emphasized that Doppler lidar fills an important role in wind power forecasts as it provides the high resolution weather observations necessary for improving forecasts made by numerical weather prediction (NWP). A scanning coherent Doppler lidar, such as the Windtracer lidar, is considered the most advantageous method of making the upstream measurements of wind profiles necessary for short-term forecasting because of its range and high resolution due to its small laser beam, which

best matches the high resolution of NWP models over a large domain compared to other measurement options such as instrumented surface weather stations. The Doppler lidar is valuable in providing ramp forecasting, a key area requiring further study. Ramps may not be captured by the very short-term NWP forecasts and will certainly not be captured by the commonly used persistence model which assumes future wind speeds are the same as the current wind speeds.

Frehlich also determined that analysis of wind speed measured by the Doppler lidar within several kilometers from the wind farm can provide the turbulence conditions which are useful for making real-time operations improvements by wind farm operators. At the time of Frehlich's publication, there were no scanning Doppler lidar field campaigns located at wind farms and the impact of complex terrain, such as an increase in wind variation increasing the spectral width, was not known. Other questions raised were whether aerosols near wind farms were sufficient for making measurements and whether atmospheric processes, for example frontal passages, make short-term forecasts possible. The current thesis involves a lidar field campaign at a wind farm in complex terrain, showing that aerosols at this wind farm location make measurements possible, and includes a study of turbulent conditions from radial velocity measurements and tracking of a ramp event due to a likely frontal passage.

Frehlich and Kelley's 2008 study of wind and turbulence profiles from lidar scans provides a comparison between lidar profiles and weather tower measurements for wind speed, direction, variance σ, turbulent eddy size L_o, and energy dissipation rate ε. This paper discussed the need for accurate measurements of turbulence profiles due to the

effects of turbulence on wind energy generation shown in previous studies. The authors noted that, with the improved statistical accuracy of the volume-averaged profiles provided by Doppler lidar measurements, sudden changes in wind conditions can be monitored, making appropriate wind farm control possible. The study used approximations of the mean wind speed for each range gate over a varying azimuth angle to determine the turbulence statistics from a best fit of a von Karman turbulence model. The authors concluded that measurements with smaller range gates would give more accurate estimates of the turbulence statistics. The authors also studied the wind speed and direction results from subsets of the data, finding the changes at different times as well as for smaller measurements regions. They found that the wind speed and direction changed based on the use of angular subsectors, which are different azimuthal sector sizes, showing spatial variability. They also found that the statistical properties degraded with the use of smaller subsectors and concluded that the statistical properties of the profiles need further study for quantification.

A study by Carpenter et. al (2013) used two Windtracer lidars, one located at a wind farm (Glacier Wind Farm) and one located to the west higher up on a mountain, further upstream. The measurements were made for 5 PPI sweeps at low elevations separated by 1° and a sixth PPI at a 45° elevation to measure the conditions at higher levels of the atmosphere. By processing the radial velocity with a sector Velocity Azimuth Display (VAD) method and propagating the wind vectors ahead to predict a future wind field, the researchers found that a direct advection model provided an improved power prediction compared to a persistence model, the method often used as a

baseline for prediction evaluation. Based on metrics of Mean Absolute Error and Standard Deviation of the absolute error, the advection model had the best result in the 10-15 minute range and gave a 40% reduction in the error for predictions as far as 45 minutes in advance.

Treinish et. al studied forecasting for the isolated wind farms located on the Canary Islands (2013). The researchers found that NWP forecasts at the islands missed most of the ramp events. They emphasized the importance of predicting ramp events for an isolated grid where the large power output variations that ramps can cause are not easily balanced. The researchers recognized a need for turbulence-scale modeling to capture the flow due to the islands' complex topography. They applied large eddy simulations (LES) and an output every 5 minutes to capture transients and integrated it with a Weather Research and Forecasting (WRF-ARW 3.3.1) model. No observation system existed so no data assimilation studies were possible. Treinish et. al are in the process of creating a training set for Machine Learning to relate modeled wind conditions to power generation based on historical data of weather forecasts and power output during ramp events and as well as a six-month continuous time period.

Wilde (2012) performed a project, also at Glacier Wind Farm, with the goal of applying off-site measurements to create short-term predictions of ramps. Ramps were defined as a change in hourly average wind farm power generation by at least 15% of installed capacity between 3 hours. The researchers set up additional measurement stations in upstream locations and used the real-time data with a Weather Research and Forecasting (WRF) model. The pressure differential with other locations was useful to

predict the ramps that will happen at the wind farm. Northern winds diverted winds coming from the more common westerly direction. The model proved better than persistence, but was not much better than existing models used at the site already. They did prove that off-site measurement stations do improve forecasting for sites with complex terrain.

2.2.2 Correlation Method

The log law, or Law of the Wall, logarithmically relates the speed of air flow to the height above ground level, and was shown in the vertical wind profile in Figure 1. The log law was considered as a prediction of wind speeds for this study according to the height above ground level. Although it is reasonable to expect that the log law will hold, it may not suitably apply to the wind profile in the Tehachapi Pass because it does not account for the mountainous terrain with wind traveling perpendicular to the ridgeline where the lidar and wind farm are located. According to Wharton, Alai & Myers (2011), the vertical wind profile may not closely follow the log law in such conditions. In their experiment, they found that the log law is more closely approximated when winds are traveling parallel to ridgelines rather than across them. The winds in their test site were predominantly moving perpendicular to the ridgelines and actually decreased as a function of height. Especially during the night, negative shear was measured such that wind speeds closer to the ground were greater than those above. A peak wind speed location was around 23 meters above the ground.

Wharton et al. (2011) also found that the energy flux did not adequately predict times of well mixed atmosphere. During the summer there was increased buoyant

sensible heat flux, but the expected well-mixed atmosphere was not seen, and instead a negative shear was measured. The complex terrain had more impact on the wind shear and turbulence than the surface energy fluxes did, which are influential in flat terrain. Therefore, it is likely that wind profiles in Tehachapi Pass will also not exhibit typical atmospheric mixing based on times of sensible energy. A correlation method is used instead to take into account the greater complexity in the relationship between wind speeds at different terrain heights.

In a study by Bilgili, Sahin, and Yasar (2007), an Artificial Neural Network (ANN) was used for wind speed prediction. A neural network is a model designed to train itself to the correlation in data sets for complex relationships that are difficult to analytically model. Historical data from 1992-1999 for a target location and surrounding reference locations that were found to have a correlation coefficient above a threshold of .59 were used to train the ANN. Successful prediction for the following two years, with a mean absolute percentage error ranging from 4.49% to 14.13% depending on the target station, showed that correlation analysis of historical wind measurements can make prediction possible without needing information on topography or other meteorological measurements. Sheela and Deepa (2013) presented a review of the available neural network techniques and showed the effectiveness of neural networks for correlation analyses.

The studies described by Sheela and Deepa use meteorological stations for the correlation. A study with lidar data opens the way for more accurate and earlier predictions by finding better correlation locations and at further locations upstream. No

papers were found that applied lidar measurement data to neural network methods for wind power prediction. This is a new route that can be taken for future expansion of this project.

Scanning Doppler lidar data near wind farms can provide high-density measurements for assimilation in high-resolution NWP models to improve smaller-scale predictions, as well as provide measurements over a large spatial extent to ANN models for statistical correlation where meteorological or topographical data is not sufficient for high-resolution NWP models. Correlations from such distributed data make predictions at each turbine possible, rather than making a single forecast for an entire wind farm empirically. Wake modeling can be used to extend the correlation prediction and model the energy content at each turbine across the wind farm, as simulated and validated with nacelle-based lidar measurements by Aitken (2014), and also as done by Adams (2014) and Hirth et. al (2014) using the concept of wind speed deficits according to the amount of energy removed from the wind by each wind turbine. The concept of using lidar data to track advection of small-scale wind structures, turbulent regions, and oncoming ramp events and to make predictions of energy content downstream is demonstrated in the current study.

Chapter 3

EXPERIMENTAL SETUP

3.1 Deployment Process

An initial test demonstration of the lidar was set up on the Arizona State University campus. After the electrical supply was connected and the lidar scanner and transceiver were carefully assembled, practice scan patterns were applied. Test data was collected to verify operability of the transceiver. A dry air purge was done for the transceiver to keep the humidity down. An extra-large socket wrench had to be attained to open the transceiver for the purge.

A remote desktop connection to the lidar's System Control Computer (SCC) was established. The remote connection was first established using a Local Area Network connection and remote control of the lidar transceiver through the SCC was confirmed. A wireless router was then set up, using a static IP address, to make remote connection possible without a Local Area Network. This was necessary for Tehachapi where the Verizon Wireless 4G internet coverage was utilized as the internet source to make remote access possible. The router required frequent refreshing by Verizon or use of an automatically refreshing webpage to keep it active.

The lidar was disassembled and shipped in a large air ride truck to provide as little vibration to the sensitive lidar equipment as possible. At the site, the lidar was reassembled by the research team. Another dry air purge was performed, and vacuum grease was acquired and applied to maintain the seal in the transceiver. Operation of the scanning patterns and the remote connection were confirmed. Two external 4-terabyte

hard drives were connected to the lidar computer and data was pushed to each of them as backup. The lidar was remotely monitored and data was collected through the remote connection and from onsite collection of the hard drives. Additional support was required from Beyond Photonics for aligning the laser optics and addressing computer errors.

3.2 Tehachapi

The second largest group of wind power generators in California is in the Tehachapi Pass, with about 5,000 wind turbines ("Tehachapi Wind Farm," n.d.). To scan the wind upstream of the wind farms in Tehachapi, the prevailing wind direction had to be found. Figure 2 shows the wind rose for June of the years 2010 through 2014, measured from the Tehachapi Municipal Airport ("Wind Roses," 2014). The prevailing wind is from the northwest.

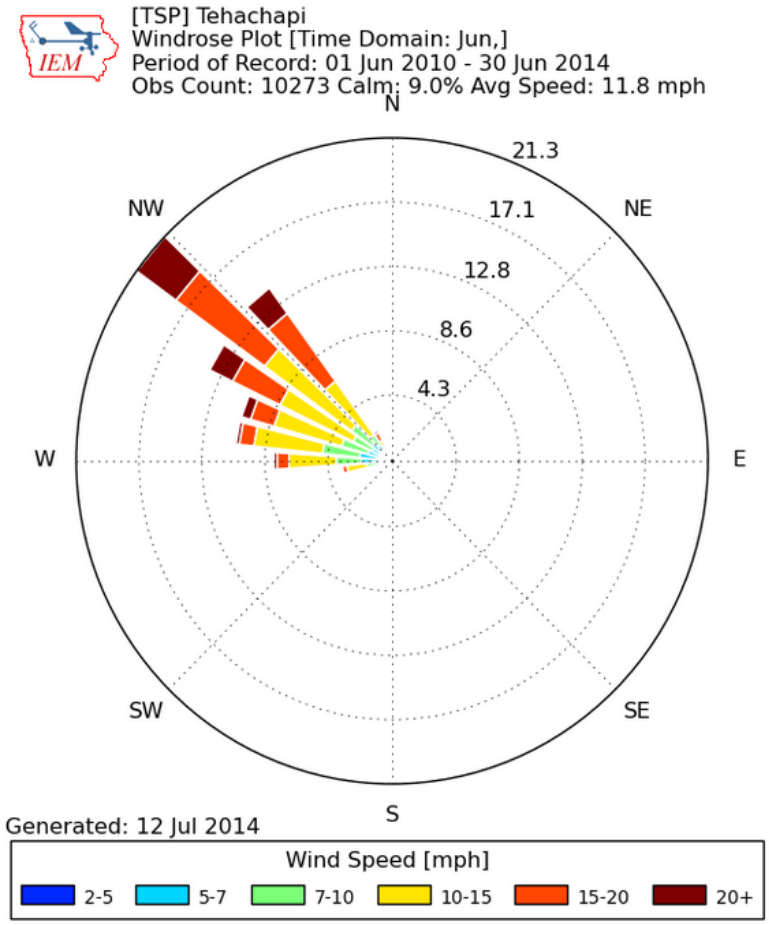

Figure 2. Wind rose for the month of June in the years 2010 through 2014. Prevailing wind is from the northwest.

Several sites in Tehachapi were evaluated for placement of the lidar. The site was chosen for visibility of the prevailing upstream (NW) direction without obstacles, proximity to an operational wind farm, and access to a secure power supply and wireless internet coverage to make a remote connection possible.

The lidar was located on the Windland, Inc. wind farm which is on a ridge at the northwest part of the Tehachapi wind farms. Figure 3 shows the topography of the Tehachapi region. The red triangle is at the location of the lidar. The y-axis increases to

the north and the x-axis increases to the east and are measured in meters according to United States Geological Survey (USGS) map topography values. To the northwest of the ridge where the lidar is located is a valley where the lidar can scan with little obstruction. To the southeast of the lidar location are the majority of the wind farms in the region.

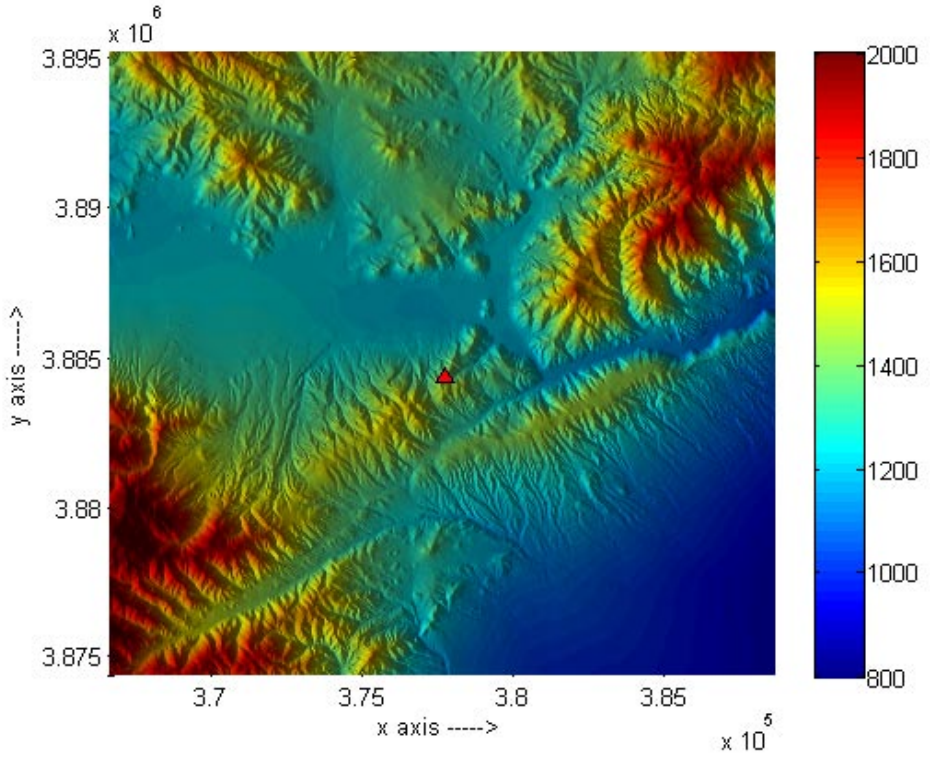

Figure 3. Tehachapi topography around the lidar, with height measured in meters. The lidar location is identified by the red triangle.

3.3 Lidar Setup

Four data sets were taken during the lidar deployment: one in March of 2014, one in early June of 2014, one in late June of 2014, and one in July of 2014. The late June dataset, June 26 to June 28, was considered most applicable to the current analysis because the other datasets included scan patterns that did not sweep the same area frequently enough, with about eight minutes separating the corresponding sweeps. The scanning pattern applied for this research from late June consisted of back and forth

sweeps between the azimuth angles of 265° and 330°, clockwise from north, at an elevation of 0°. The beginning of each consecutive sweep is separated by approximately 30 seconds.

For a wind speed of 14 m/s, the distance of advection over 30 seconds, the time between sweeps, is approximately 420 meters. Future experiments should use repeating, rather than back and forth, scans to have a consistent time step between data at each location and should repeat the sweep frequently enough that the distance of advection is sufficiently smaller than the extent of the measured region. For a measured region of 10 kilometers along the mean wind direction and an advection distance of 420 meters, advection of a durable structure can be tracked for about 24 sweeps.

Figure 4 shows the region that is scanned by the lidar for this dataset relative to the topography of Tehachapi. The photo in Figure 5 shows the view to the northwest, in the direction of the scan, from the location of the lidar at the wind farm.

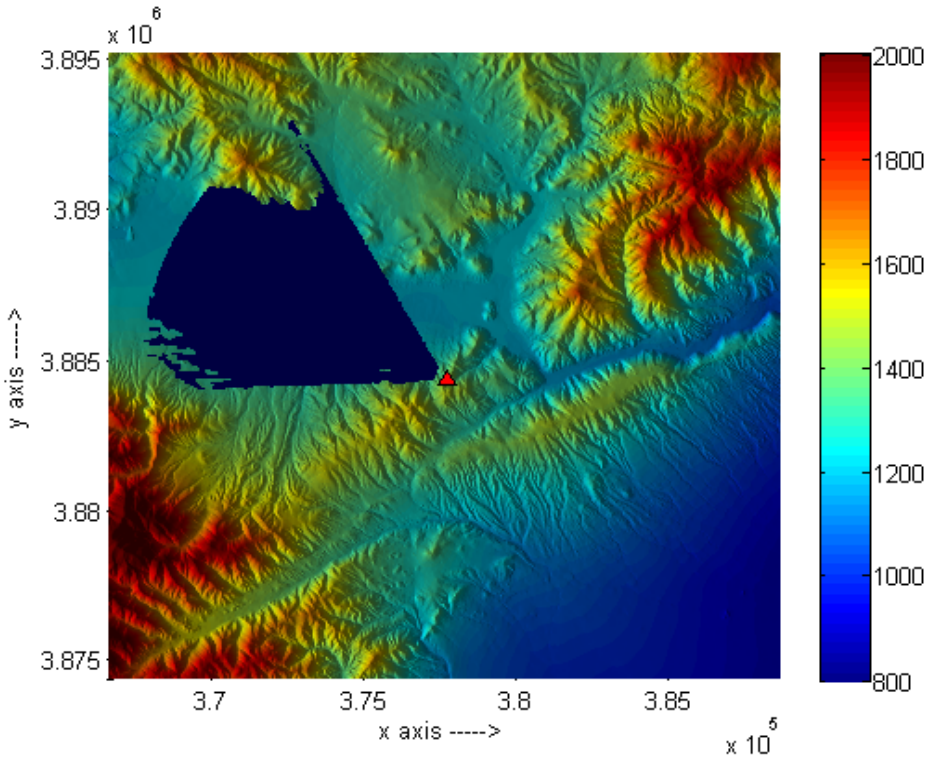

Figure 4. The sweep region (dark blue sector) shown over the Tehachapi topography, with a scale measuring the ground level elevation in meters above sea level. The lidar location is identified by the red triangle.

Figure 5. Photo of view to the northwest, where the upstream scan is performed, from the lidar location.

The scan was made over the city of Tehachapi, which is at an altitude of about 1220 meters, from the wind farm on a ridge at an altitude of about 1450 meters. Mountains can be seen at either side of the scan, which create a mountain pass through which the wind travels. The mountains visible in the photo can be seen as obstructions in the scan as shown earlier in Figure 4. In Figure 6, the location where the lidar was placed, at the base of a lattice tower wind turbine which provided the electrical supply, can be seen.

Figure 6. Photo showing the lidar location and the view to the southeast.

The photo in Figure 6 shows the view to the southeast, toward the large nearby wind turbines, downstream of the lidar location. Additionally, many more wind farms are also further to the southeast of the lidar's location.

Chapter 4

ANALYSIS

4.1 Volume Velocity Processing and Sector VAD

It would be desirable to have the magnitude of the wind speed and the direction to determine the power output by a wind turbine. However, the lidar only provides measurements of component velocities in the radial direction around the lidar. The radial velocity, v_r, measured by the lidar depends on u, v, and w, the orthogonal components of the wind in the x, y, and z directions, and the azimuth and elevation angles, θ and ϕ, of the line of sight, and is given by

$$v_r = u\cos\theta\cos\phi + v\sin\theta\cos\phi + w\sin\phi \quad (2)$$

In order to determine the magnitude and direction of the wind, assumptions must be made to retrieve the two horizontal orthogonal components from radial velocity. At low elevation angles, for which $\sin\phi \sim 0$, the component of the wind in the z-direction, w, is assumed to be negligible (Krishnamurthy, 2013, p. 22). The orthogonal components u and v were retrieved mathematically by the Volume Velocity Processing (VVP) method, which assumes a linear function can be used to approximate the analysis volume (Krishnamurthy, 2013, p. 21) for each volume of the scan that has a small change in range, azimuth angle, and elevation angle. The assumption is made that all of the radial velocity vectors in the volume approximately represent one single actual velocity vector that is constant over the volume. In this way, independent information is provided by each of the radial vectors in the volume since they show components of the overall velocity from nonparallel directions. Single Value Decomposition is performed on a

matrix of values from each point in the volume and a least squares method is applied to determine a best fit for the overall velocity in each volume of the scan (for additional details, see Krishnamurthy, 2013, p. 21).

The radial velocities determined by the lidar from the Doppler frequency shift were plotted and animated with time to depict the radial velocity time series. In order to study the magnitude of the wind speed throughout the region, the radial velocities were decomposed into components in orthogonal directions x and y, parallel to the ground. Since the data set did not contain any measurements at a second elevation, it was necessary to modify the VVP formulation to only use data from one sweep, such that it actually processed the velocity within an area. As a result, the retrieval that was applied for this study is considered a sector Velocity Azimuth Display (VAD) method. The measurements were made at a 0° elevation, so any vertical components of velocity are tangential to the lidar's line of sight and do not contribute to the radial velocity.

4.2 Virtual Projected Wind Farm and Correlation

The concept of a virtual projected wind farm involves simulating the power output of turbines as though they are part of a wind farm that is located upstream. This determines the extractable energy content in the upstream wind and can be used to give a prediction of the power output when the wind reaches the actual wind farm. The prediction is created based on a function of how the energy content changes as the wind features advect toward the actual wind farm. The time required for advection at the mean wind speed over the distance between the upstream and downstream locations was considered to be the time shift between the wind profiles. This makes the simplifying

assumption that the time shift is constant over the time period, although in reality it will depend on the changing speed of the wind. The best fit between a direct relationship, a linear relationship, and a second order polynomial relationship was then determined to correlate the wind speeds at each upstream location. The linear fit was evaluated by Matlab by the 'poly1' fit function, the second order polynomial fit was determined by the 'poly2' fit function, and higher order fits were evaluated by the 'fit' function with the respective order defined as an input. Predictions based on additional time periods were made by applying the analyzed fit to the upstream time series as a function. The predictions were evaluated using Mean Absolute Error and standard deviation of the absolute error calculations.

4.3 Discussion of Assumptions and Potential Sources of Error

Negative radial velocity measurements represent movement toward the lidar, according to standard procedures for remote sensing. For this experiment, the velocities reported by the lidar were positive for radial measurements to the northwest, representing movement from the southeast, away from the lidar. This was in the opposite direction as those reported by the National Oceanic and Atmospheric Administration (NOAA) for local weather data from the Tehachapi Airport ("NOAA National Climatic Data Center," n.d.). NOAA reported that the wind was coming from about 300° clockwise from north, meaning that the upstream direction was to the northwest. Figure 7 shows the wind speed and direction measured by NOAA for June 27 GMT.

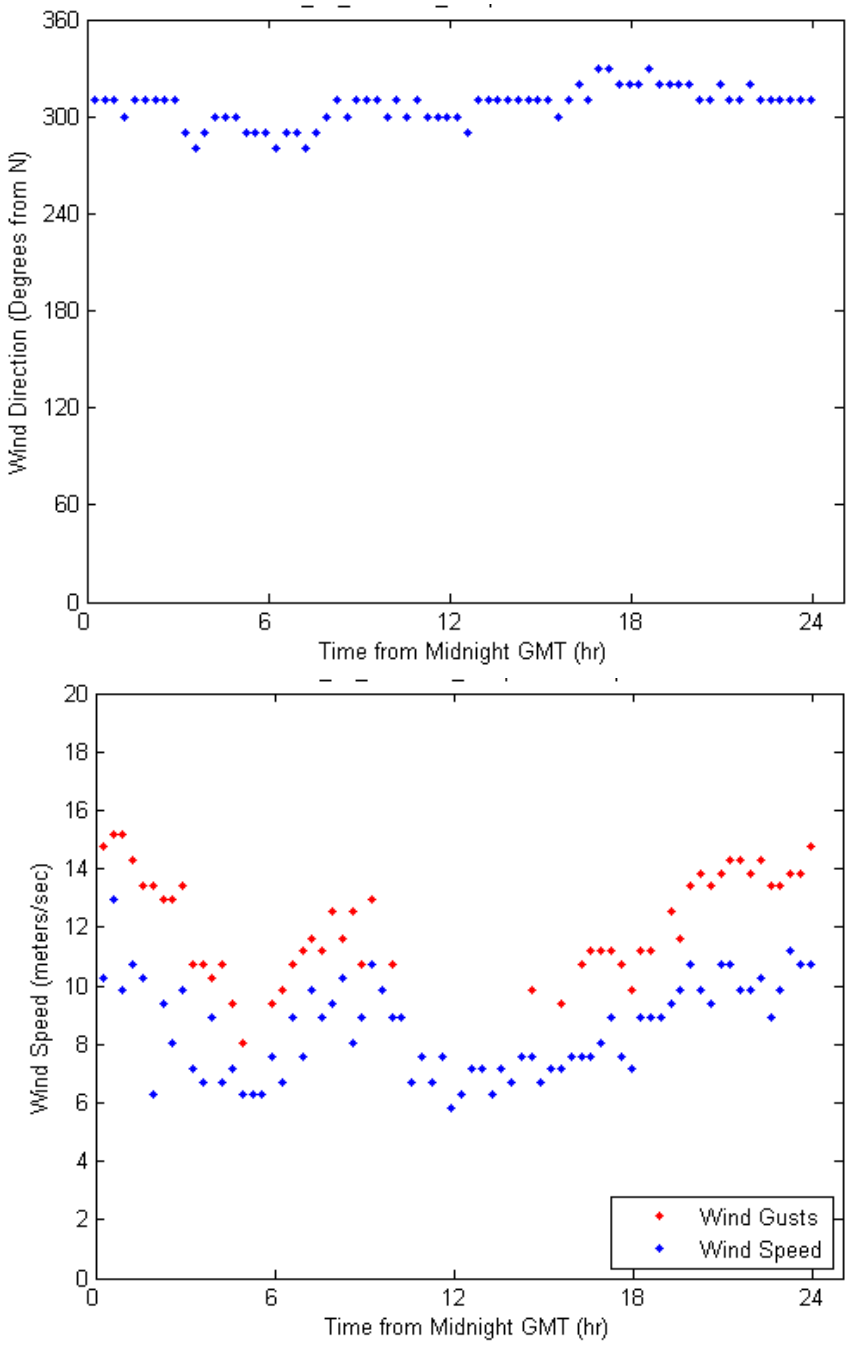

Figure 7. Wind Measurement at Tehachapi Airport at 1219 meter elevation for June 27 in GMT, adapted from NOAA ("NOAA National Climatic Data Center," n.d.). (Top) Wind direction clockwise from north. (Bottom) Wind velocity and gusts.

It was also noted that the magnitude of the NOAA wind speeds is lower than those reported by the lidar. This is likely due to the measurements being taken near the ground at the Tehachapi airport, which is in the valley and has an elevation of 1219 m. Meanwhile, the lidar was situated on a mountain ridge and took measurements at 0° elevation at 1450m across the valley, observing wind that has less of a frictional effect from the ground. It was determined that, based on the comparison with NOAA, inspection of the direction of advecting structures in plots created from the radial velocity, and responses from the lidar manufacturer that implied the lidar could have a reversed value as part of its spectral analysis, it would be assumed for this research study that the radial velocities were reported in reverse by the lidar, so all values were multiplied by -1. The framework developed in this study would be applicable to any wind direction for which measurements are made along the mean wind direction. Future work using lidar should include a comparison with collocated measurements from a validated instrument, such as an anemometer, to confirm the lidar's output. Such data was not available for this study.

Working with lidar data involves error associated with the instrumentation, the retrieval, and the data analysis. It is important to consider the sources and magnitudes of the error introduced by each portion of the experiment to understand how accurate the results will be.

The lidar itself has limitations in its accuracy. The spatial and temporal accuracy are dependent on the measurement technique as well as the internal mechanisms and clock in the lidar. The radial velocity that is measured by the lidar is not measured just at

a point in space, but is the average radial velocity determined by backscatter of each particle along the lidar beam within a range gate, which is a distance measured radially from the lidar. The range gate used in this experiment was 100 meters. The volume of the atmosphere that is sampled at each successive range gate increases as the laser beam diverges, although as a coherent laser beam, there is expected to be little divergence of the beam (Hutton, 2008). The distance between successive azimuthal measurements increases at range gates further from the lidar since the chord-length of a circular sector with a constant interior angle increases with distance from the center. The spatial resolution therefore decreases with each range gate away from the lidar. According to Table 1, from the handbook for the lidar, the spatial resolution is typically from 100x100m to 200x400m (Hutton, 2008). In addition to being an averaged quantity, the velocity measured by the lidar has a level of error. The radial velocity has an accuracy of 0.5-1 m/s according to the handbook (Hutton, 2008). The measurements made by the lidar are therefore accurate to this amount. The radial velocity measurements made in the prevailing wind direction were compared with NOAA data from a nearby location to show that the measurements are reasonable. The consistency of the lidar's measurements shows that the lidar instrumentation has reasonable precision, as well.

The data analysis process also introduces sources of error. The truncation error associated in any computational analysis is present. It is dependent on the properties of the computer, which in this case was a 64-bit operating system, as well as the calculations that are done. For example, the effect of truncation error may have been recognized when squared radial velocity measurements were subtracted from each other to find the change

in kinetic energy between sweeps. The radial velocities measured near the mountains on both ends of the sweep were very small and were also close together due to the sweeping back and forth motion of the scan pattern, which covered the area at a very small time difference. The result alternated between positive and negative values that were not reasonable. This was mitigated when every other sweep was removed such that there was an equal time step between each beam of the consecutive remaining sweeps and there were sufficient differences between sweeps at these locations. These regions of small radial velocity were also excluded from the correlation analysis because their radial directions were not in the prevailing wind direction.

Interpolation was used to collocate the points from successive sweeps, so that error was introduced due to the interpolation. Since the data for each range gate is an average of all values taken in that region, interpolation compounds the error due to the limited spatial resolution. For the input to the turbine model, the radial velocity data was interpolated over time by location at each time step that had any missing data points. The output of the model was resampled to provide data points at approximately one-minute time steps.

The correlation process for predicting wind speeds compounds error due to the spatial and temporal resolution. The correlation itself fits data to make the prediction and therefore contains additional error. The implementation of Euler's method that is suggested as a way to predict movement of wind structures introduces an error dependent on the time step between data points. The data applied has a time step of approximately 30 seconds, therefore leading to errors on the order of 30 seconds. There are also physical

errors that are included in the prediction. The lidar measures the radial velocity but does not measure other physical properties. Effects on wind velocity due to local conditions are neglected as a result. The assumption is therefore made that, over the time period and region of measurement, the air density, viscosity, temperature, and atmospheric stability are constant.

One of the methods used in the analysis is retrieval of the radial velocity into two-dimensional Cartesian coordinates, called sector VAD processing. This method involves assuming homogeneity over each sector of the region as well as neglecting any vertical component of velocity. The small-scale characteristics of the flow are not resolved with this method. Due to the complex topography of the Tehachapi Pass region used for this experiment, the assumptions may not be valid, though the result of this analysis may give useful information about the large-scale flows in the region.

The evaluation of extractable energy content according to the wind speed includes error due to the model that is used. The model takes into account turbine parameters from NREL to determine the power produced at a certain wind speed, however the model will not necessarily represent an actual wind turbine that has variations from the ideal case. It also makes the assumption that the turbine has instantaneous yawing into the wind which is idealized since there is some delay in actual wind turbines.

Chapter 5

RESULTS AND DISCUSSION

5.1 Advection

The analysis focused on whether Doppler lidar can make measurements that provide information for useful short-term forecasts and can make it possible to track changes in the energy content of the wind as it moves toward the wind farm. To do this, data collected during the deployment was studied for temporal and spatial correlation between upstream and downstream. Visual inspection of radial velocity plots from each sweep showed that there are visible structures that can be recognized and tracked moving toward the lidar. This inspection suggested that a mathematical correlation exists between the upstream energy content and the energy content downstream after a time shift.

An example of the plotted radial velocity showing a structure advecting that can be easily tracked visually is shown in Figure 8 and Figure 9. The example structure is identified by its recognizable shape, as it is shaped like a ‘V.’ In Figure 8, the location of the V in the sweep can be seen. Figure 9 shows the movement of the structure, enclosed in the black box for convenience. The sweeps that are shown are approximately one minute apart and were all made by a counterclockwise sweep so that all corresponding parts of the images are at a consistent time step. The shape and magnitude of the structure are maintained throughout the region. This structure represents a high speed area in the wind that could cause an increase in wind power output when it reaches the farm. Advanced knowledge of such structures could provide wind farm operators with information about impending changes in energy content.

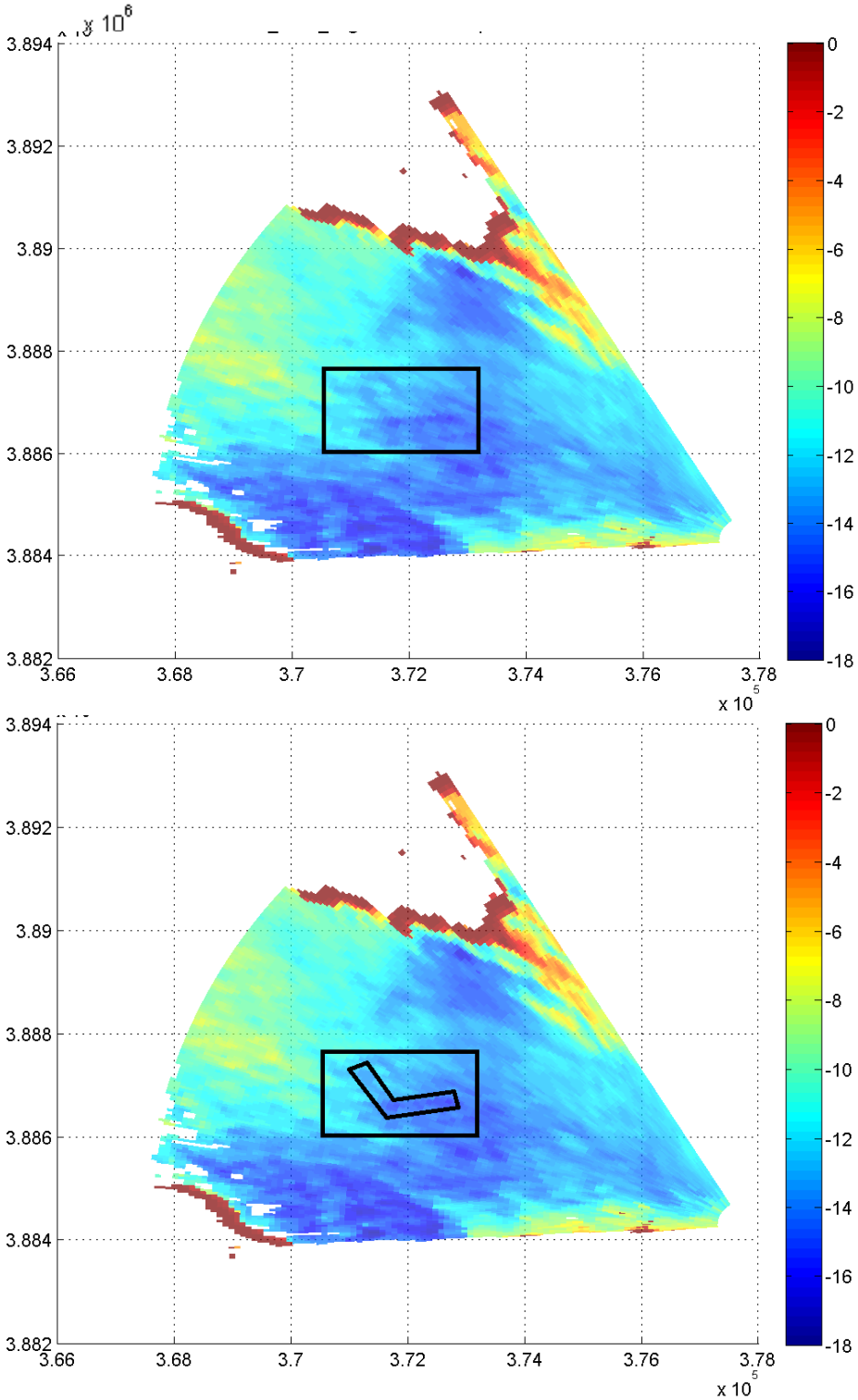

Figure 8. V-shaped high speed structure, with and without the structure identified by the black 'V' shape. June 27 12:09 GMT. The colorbar gives measurements in m/s, and positive values represent movement away from the lidar along its line of sight.

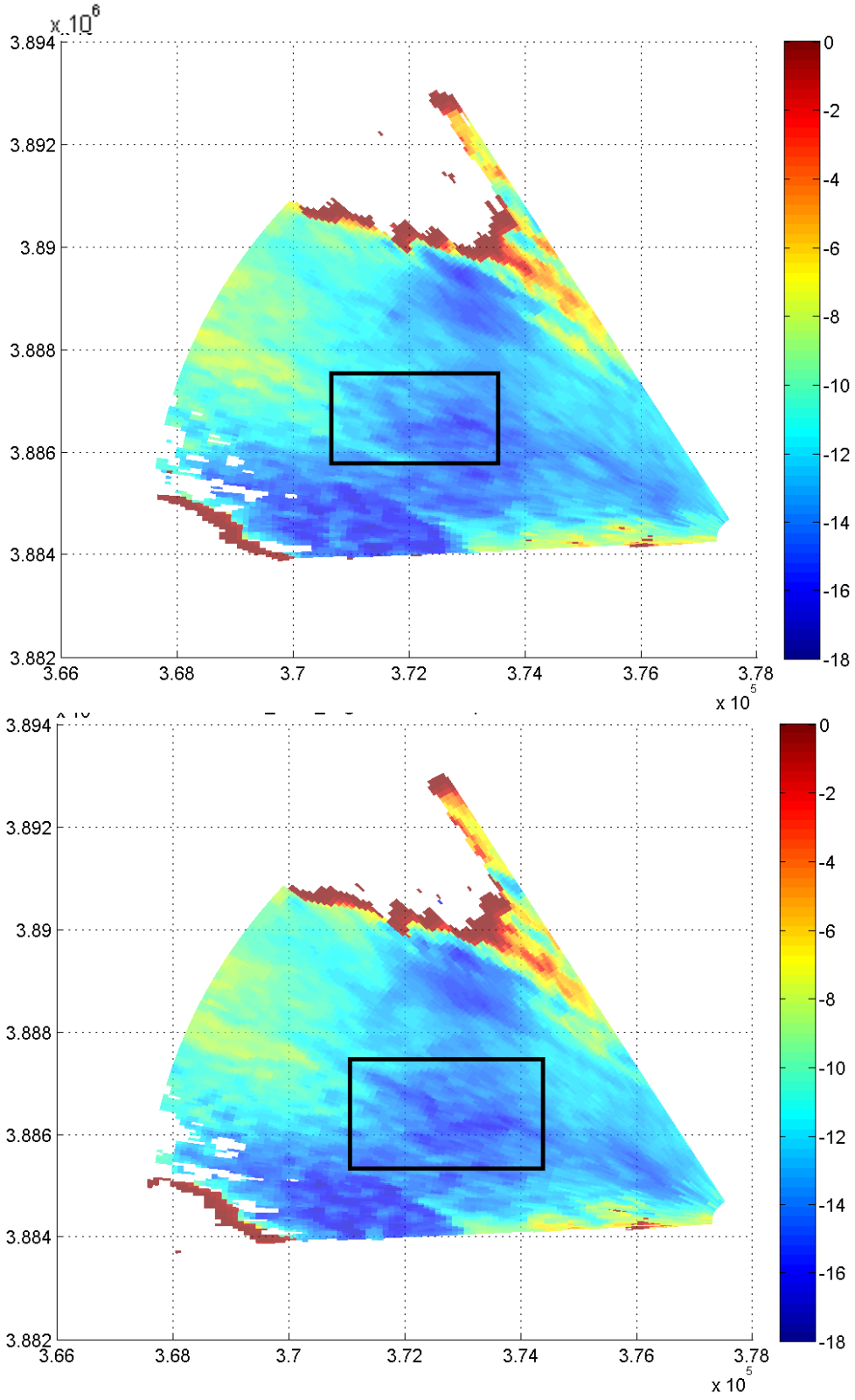
x 10^6
3.894
3.892
3.89
3.888
3.886
3.884
3.882
3.66
3.68
3.7
3.72
3.74
3.76
3.78
x 10^5
0
-2
-4
-6
-8
-10
-12
-14
-16
-18

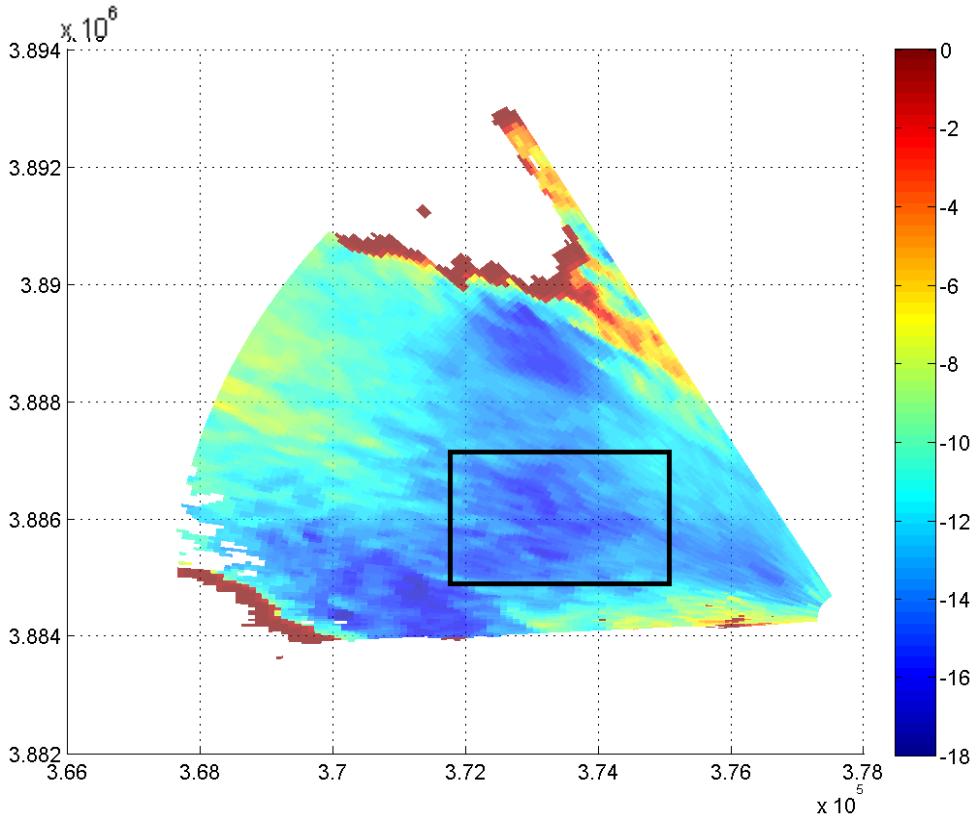

Figure 9. V-shaped structure advecting along the radial direction. First image is at GMT 12:09:30, with about 1 minute between each following image. The colorbar is in m/s and positive values represent movement away from the lidar along its line of sight.

The average advection speed, U, can be determined by the distance traveled, ΔD, during a given time period, τ.

$$U = \frac{\Delta D}{\tau} \tag{3}$$

The distance traveled over the time period, or the advection distance, is measured to be about 2,275 meters for sweeps separated by a time period of about 2 minutes and 26 seconds. The advection speed is calculated to be about 15.6 m/s which is similar to the wind speeds measured, showing that the structure can be tracked as it advects with the speed of the wind.

The magnitude and direction of the wind at each location can be determined from the radial velocity using retrieval methods. When performing the retrieval, data near hard targets should be removed to avoid erroneous results. This can be done by filtering the data that have high values of backscatter. The data near the mountains that obstruct the scans needed to be removed for this experiment. The backscatter, showing the high values near the mountains, is presented in Figure 10. The backscatter was calculated at each range gate, at a distance r from the lidar, from the Signal-to-Noise ratio (SNR) measured in decibels, by the following formula (Hutton, 2008).

$$Backscatter = SNR \times r^2 \tag{4}$$

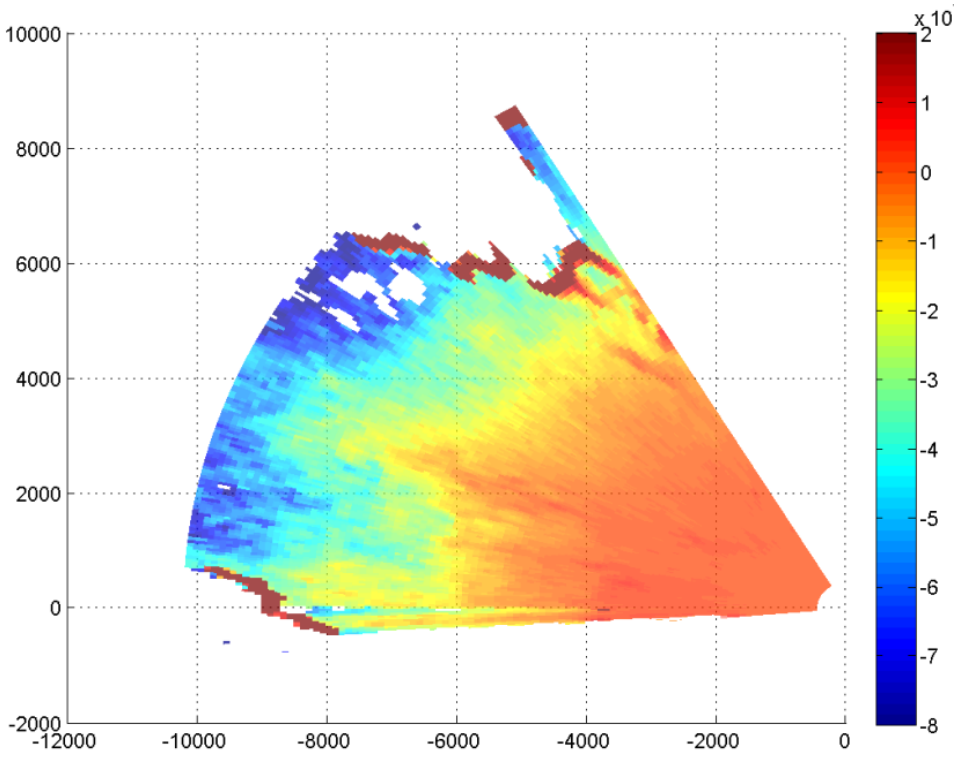

Figure 10. Backscatter. High values are recorded near the hard targets.

The sector VAD retrieval method was applied for this study due to the scan pattern of a single Plan Position Indicator at 0° elevation. An example vector field resulting from the retrieval is provided in Figure 11. Sectors with a 30° azimuth were used. This sector size was necessary to ensure that the retrieval method did not experience mathematical instability, which was seen at lower sector sizes by unrealistically high retrieved velocities and overlapping velocity directions. However, this retrieval method uses data at surrounding points in the sector to determine the velocity based on a least-squares approximation. As a result, with larger sector sizes the velocity field becomes increasingly uniform. The 30° sector size was chosen to balance these effects for stability as well as maintaining the non-uniformity of the vector field.

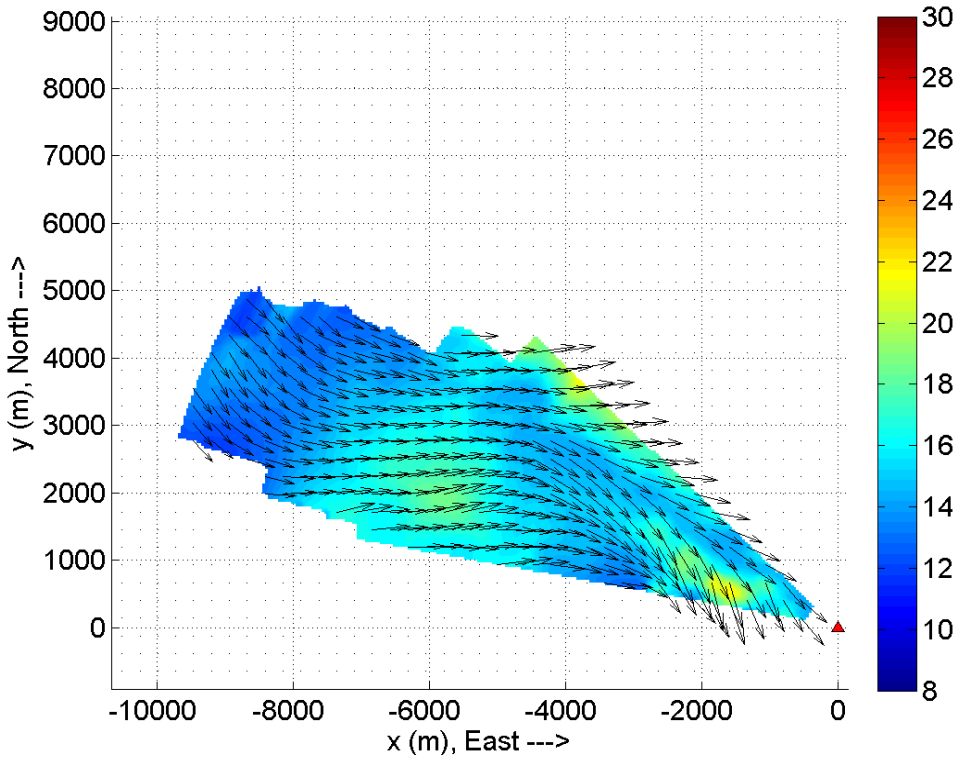

Figure 11. Retrieved velocity field for June 27 09:09 GMT. Regions with hard targets were removed. The colorbar gives wind magnitude in m/s.

With the vectors of wind speed at each location, the direction of advection can be evaluated. Using the assumption that the direction of the wind vectors over the scanned region is consistent over time, streamlines can be created in the wind field. In Figure 12, the velocity field from July 27 09:23 GMT can be seen to be consistent compared to that of Figure 11.

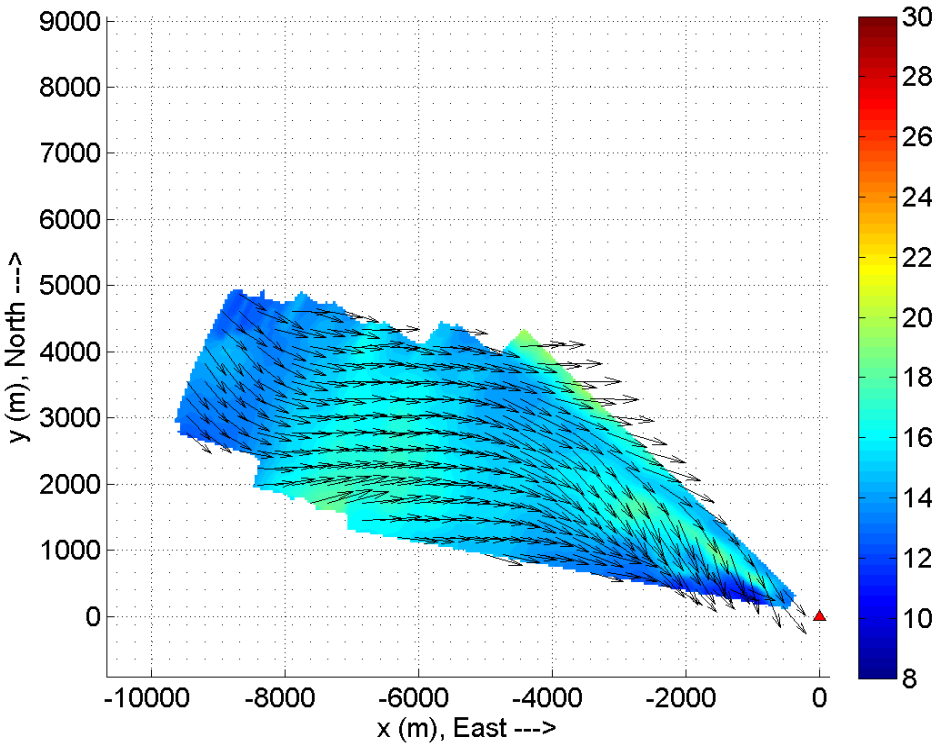

Figure 12. Retrieved velocity field for June 27 09:23 GMT. Regions with hard targets were removed. The colorbar gives wind magnitude in m/s.

The streamlines provide an estimation of the path that the wind takes to move downstream. For a given downstream location, the nearest streamline can be traced back to determine an upstream location. This location experiences the wind that will advect to the downstream location, and can be used to give a short-term prediction of the wind speeds that will be seen downstream. The streamlines can be updated over time to find

the real-time upstream location, based on this assumption of a consistent wind field over the time period of advection. For this study, the streamlines remained mostly consistent over the measured time period from GMT 11:48 to 12:33. The streamlines for the velocity field approximately 20 minutes apart are shown in Figure 13.

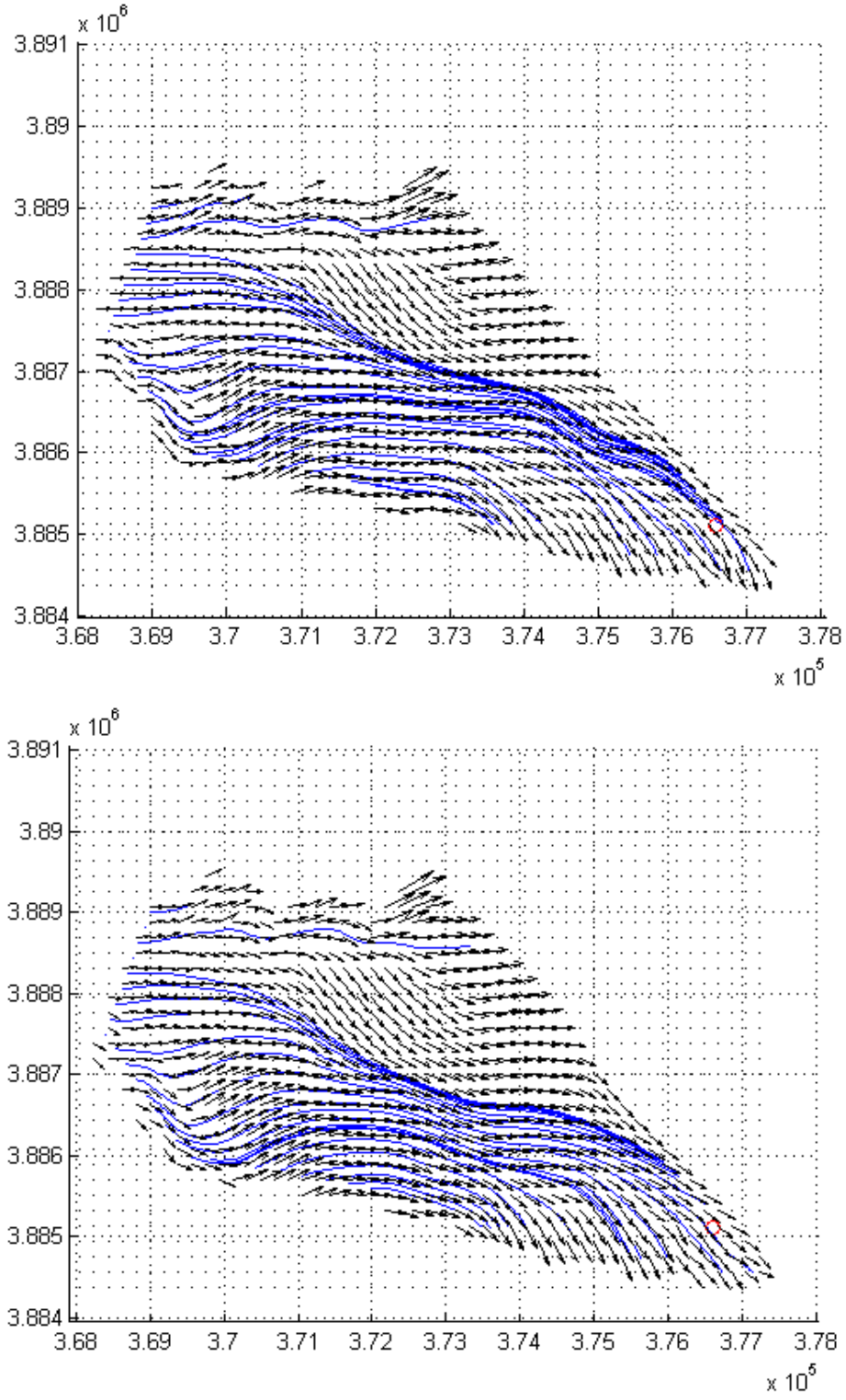

Figure 13. Streamlines over retrieved velocity field at (top) GMT 11:51 and (bottom) GMT 12:10 on July 27.

A selected location, marked by a red circle, was considered the ‘downstream’ location. The streamlines were traced back from this point. Since the streamlines from this point are approximately along the radial direction at the center of the scan, locations along the radial direction at 296 degrees clockwise from north were used for the correlation and prediction. The locations along this radial direction are shown in Figure 14, where the downstream location has a large marker and each upstream location is about 670 meters further away.

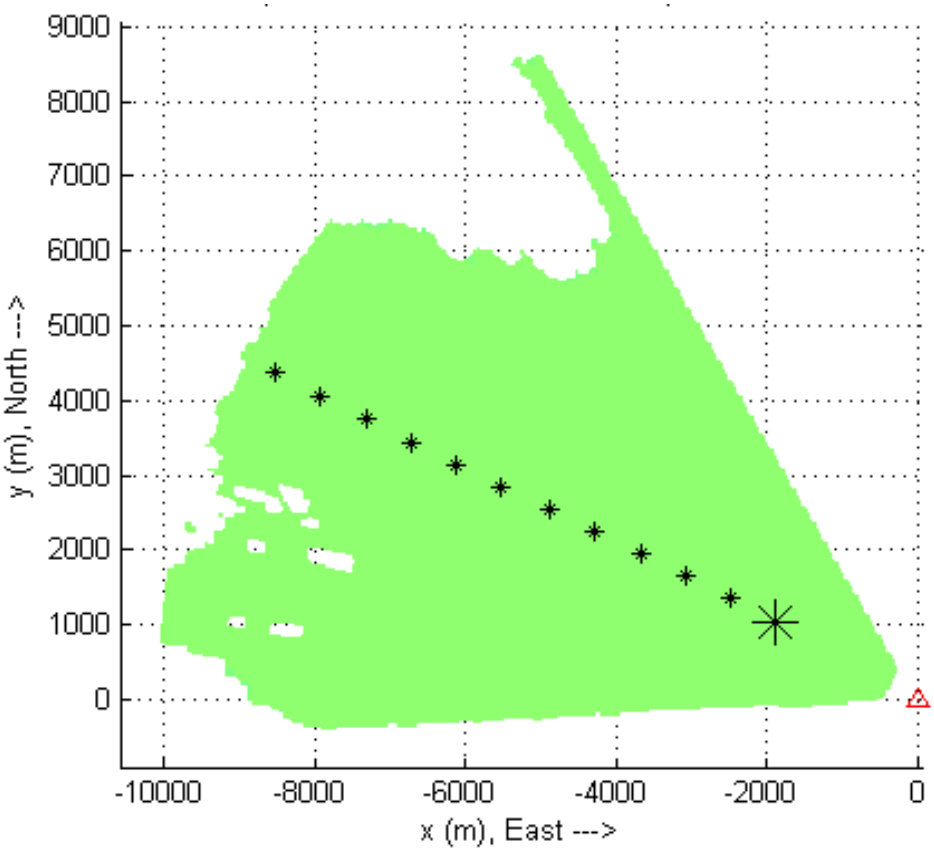

Figure 14. Selected locations along radial direction for correlation study. Large marker indicates the ‘downstream’ location. Markers are about 670 meters apart. The lidar is indicated by the red triangle.

A radial direction at the center of the scan was important because it means that each sample is at a consistent time step, while near the edges each time step alternates between large and small due to the back and forth scanning pattern that was used by the lidar.

An important parameter for wind forecasting is the variance in the wind, or dispersion of the speed about the mean speed, which quantifies the intensity of turbulence (Atkins, 2001). The variance can be used to determine the Turbulent Kinetic Energy (TKE), a parameter frequently used to study turbulence. According to Taylor's Hypothesis, with the assumption of a frozen turbulence field, the time scale of the turbulence is related to the length of the eddies making up the turbulence field (Atkins, 2007). Based on this concept, the variance was measured according to the wind speeds over space, in place of measuring them over time, and was defined as the spatial variance along a streamline. The difference between the value at an upstream point and the mean over an appropriate length scale along the streamline is calculated. The intensity of the turbulence as it advects can therefore be determined, and regions of high turbulence can be seen as they move toward the wind farm. The oncoming turbulence is important for wind farm operators to apply control methods such as blade pitching to their turbines to minimize loading. With this method, regions of higher turbulence can be forecasted.

TKE is calculated by first calculating the mean wind speed over the time period. The following equations provide the formula for calculating the mean of a variable, A, over a given time period,

$$\mathrm{N} = \frac{T}{\Delta \mathrm{t}} + 1 \tag{5}$$

$$\overline{\mathrm{A}} = \frac{1}{N}\sum_{\mathrm{i}=0}^{\mathrm{N}-1}\mathrm{A_i} \tag{6}$$

where N is the number of samples in the time period, T, and Δt is the time step between sampled measurements. Variance, σ_A^2, is the dispersion about a mean value A. With N as the number of points in the dataset, the variance can be calculated according to the following formula.

$$\sigma_A^2 = \frac{1}{N}\sum_{\mathrm{i}=0}^{\mathrm{N}-1}(\mathrm{A_i} - \overline{\mathrm{A}})^2 = \overline{\mathrm{a}'^2} \tag{7}$$

Taking u, v, and w to be the orthogonal components of the velocity, TKE per unit mass is calculated by the following equation (Šavli, 2012).

$$\frac{TKE}{mass} = \frac{1}{2}\left(\overline{\mathrm{u}'^2} + \overline{\mathrm{v}'^2} + \overline{\mathrm{w}'^2}\right) \tag{8}$$

The spatial variance along the streamline can be determined in a similar fashion based on the assumption that the mean value of the previous time period can be approximated by the mean value of the points downstream of the location. The time period corresponding to a given advection distance is determined by

$$T = \Delta D \times U \tag{9}$$

where T is the time period, ΔD is the distance between locations, and U is the wind speed. N is the number of sampled data points along the streamline that correspond to the time shift for the selected advection distance, used to calculate the spatial mean of the radial velocity, $\overline{RV}$.

$$\mathrm{N} = \frac{\Delta \mathrm{D} \times \mathrm{U}}{\Delta \mathrm{t}} + 1 \tag{10}$$

$$\overline{RV} = \frac{1}{N} \sum_{\mathrm{i}=0}^{\mathrm{N}-1} RV_{\mathrm{i}} \tag{11}$$

For this dataset, 1 kilometer was chosen, an advection distance corresponding to about 71 seconds for a mean wind speed of 14 m/s. For TKE calculations, an average on the order of thirty minutes is recommended to separate the turbulence from the mean wind component (Šavli, 2012). The spatial variance is being calculated on a smaller length scale to show the turbulent fluctuation structures as they advect toward the wind farm. The spatial variance, or variation from the mean, along the streamline, gives the turbulence intensity. The formula used for the spatial variance at a point along the streamline with respect to the measured radial velocity, RV, is

$$(RV - \overline{RV})^2 = rv'^2 \tag{12}$$

This could be calculated for a range of points to find the variance over a spatial range corresponding to a time period of interest, by

$$\sigma_{RV}^2 = \frac{1}{N} \sum_{\mathrm{i}=0}^{\mathrm{N}-1} (RV_{\mathrm{i}} - \overline{RV})^2 = \overline{rv'^2} \tag{13}$$

The turbulence intensity, rv'^2, was plotted with time as a representative value of the TKE given by this spatial variance. Figure 15 shows a series of plots of this spatial variance, from sweeps one minute apart. It can be seen that the high turbulence structures can be tracked as they move from the northwest closer to the lidar location at the wind farm.

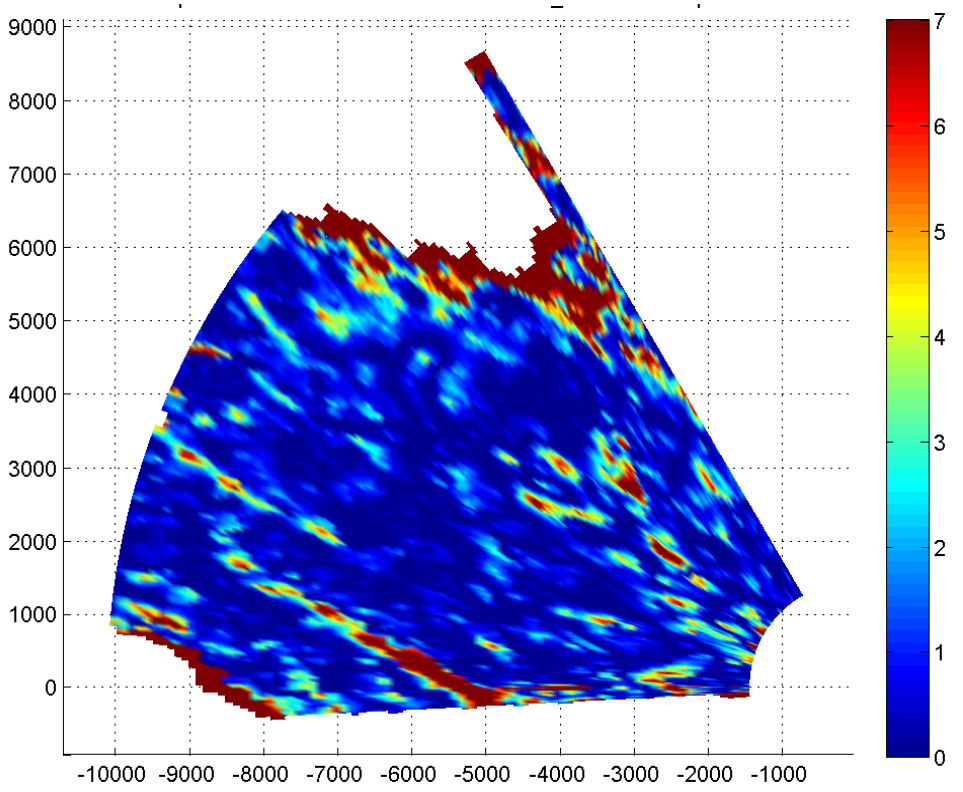
9000
8000
7000
6000
5000
4000
3000
2000
1000
0
-10000 -9000 -8000 -7000 -6000 -5000 -4000 -3000 -2000 -1000
7
6
5
4
3
2
1
0

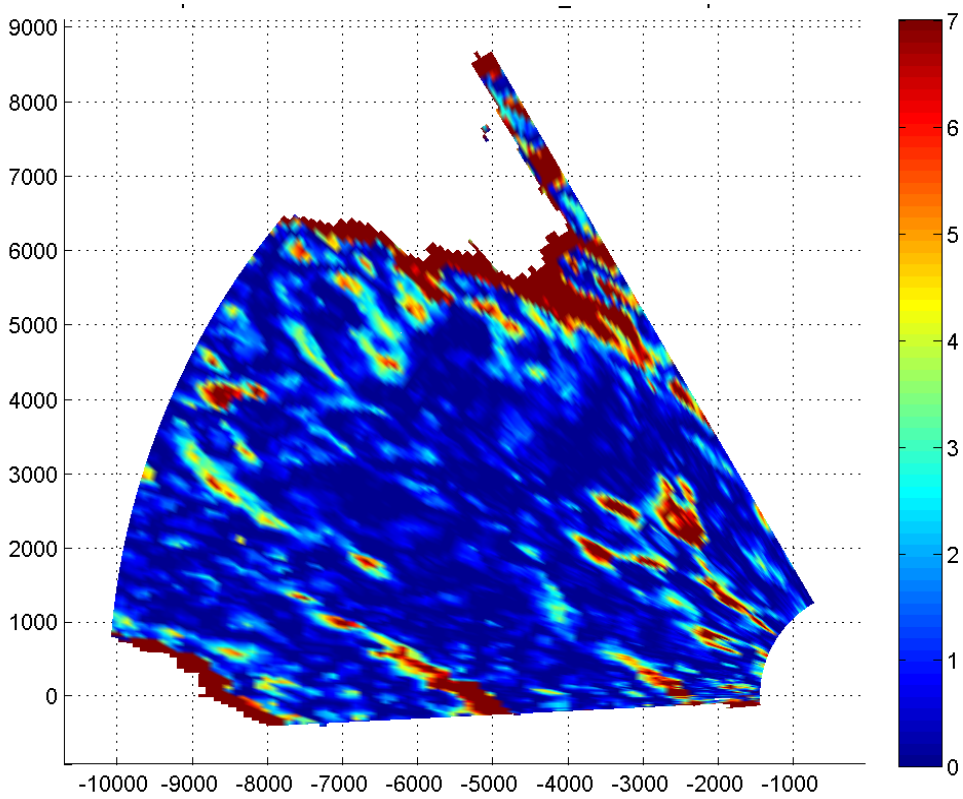
9000
8000
7000
6000
5000
4000
3000
2000
1000
0
-10000 -9000 -8000 -7000 -6000 -5000 -4000 -3000 -2000 -1000
7
6
5
4
3
2
1
0

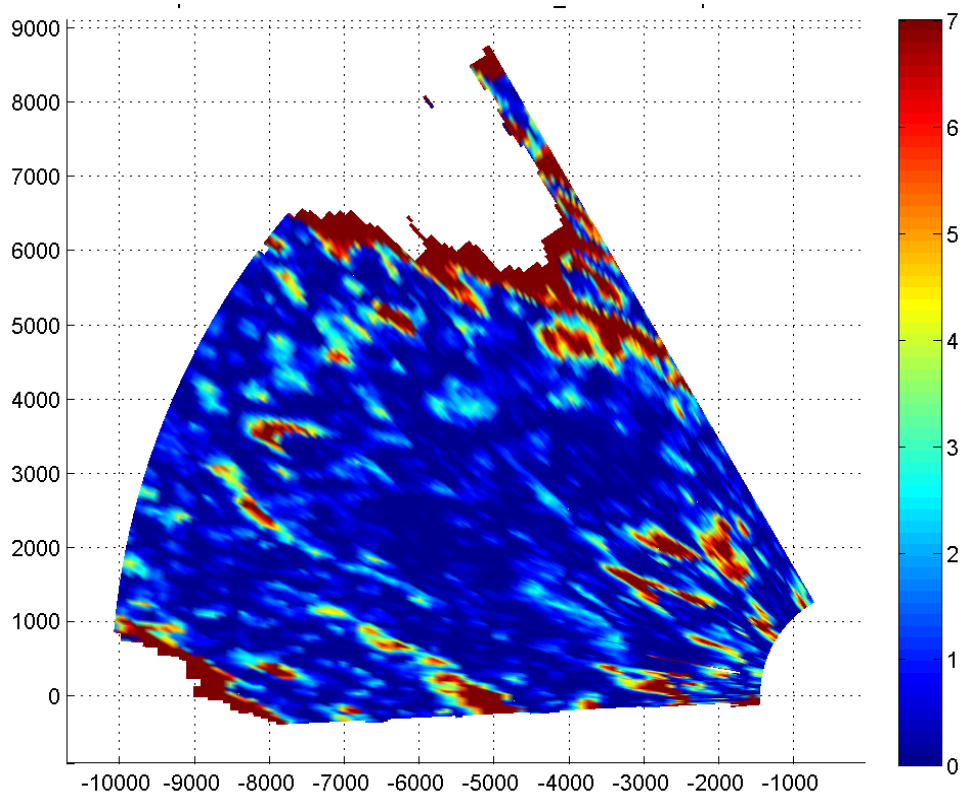

Figure 15. Spatial variance for 1 kilometer advection distance. Sweeps at 1 minute apart are shown, each with lidar scans in the same clockwise direction to show equivalent time steps at each location. These sweeps are taken at about 02:38 to 02:40 July 27 GMT.

Therefore, the advection of the turbulent structures can be monitored. This information would be useful to the wind farm operators as they could know in advance about times of turbulence for their wind turbines and the length of the turbulent patch to make proper preparations.

5.2 Energy Content

The extractable energy content of the wind is the actual power that can be generated from the wind by a real wind turbine. It is also important to wind farm operators to have advance knowledge of the power that they will be able to generate from

the wind. The energy content can be evaluated by creating a ‘virtual wind farm’ in the upstream wind. This is done by modeling the output of turbines at the true wind farm as though they are experiencing the wind at the upstream location. With this ‘projected’ energy content, a correlation can be found that relates the upstream profile to the wind power that can be generated at the wind farm after advection.

A Simulink model of a 5MW wind turbine from NREL specifications (Krishmanurthy et. al, 2013; Jonkman et al, 2007) determines the power that can be produced by the turbine from a given wind speed time series. The turbine has a cut-in wind speed of 3 m/s, a rated wind speed of 11.4 m/s for its nameplate power output of 5 MW, and a cut-out wind speed of 25 m/s.

The Simulink model was given example speeds to display its reactions, shown in Figure 16.

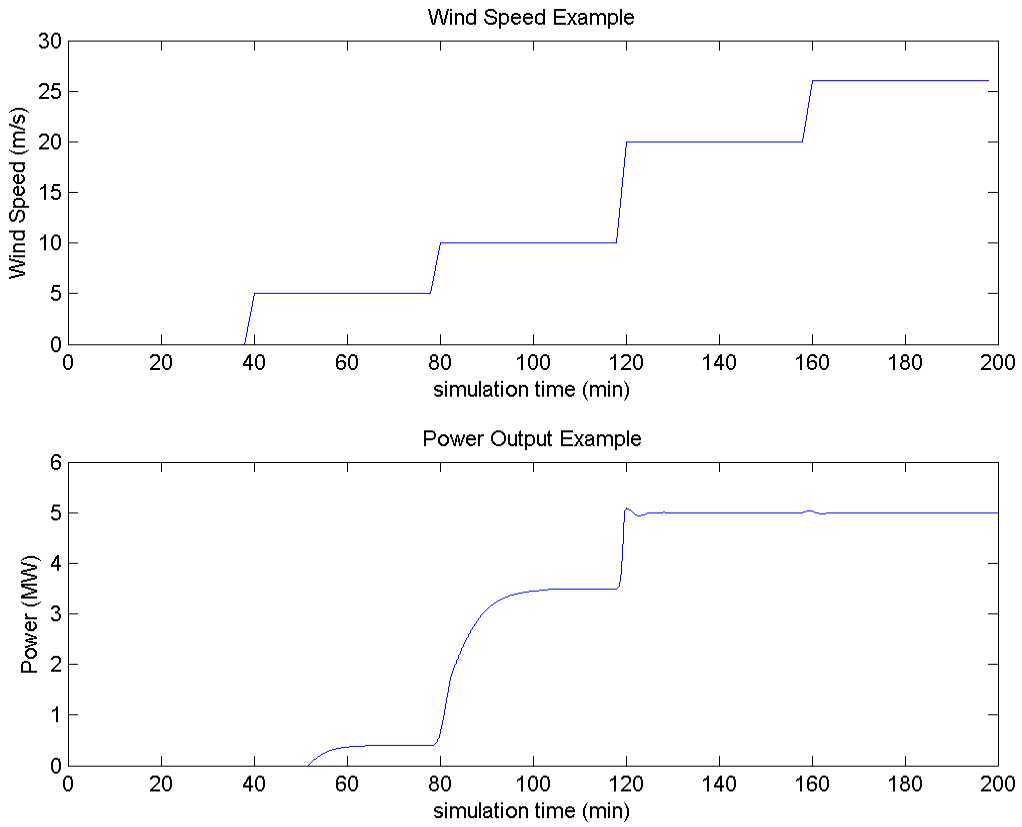

Figure 16. The power output (bottom) based on an example wind speed profile (top) for the modeled NREL 5 MW turbine from Simulink.

The model output has a delay time for increases in wind speed, as would be expected in the output of an actual wind turbine. The model does not exhibit a cut-out point; however that will not affect the results of the current study since the lidar measurements were limited to 20 m/s. The model required an input wind speed profile with a value at equally spaced time intervals. Since some of the profiles of wind speed measured by the lidar contained missing values, due to speeds over 20 m/s and to measurements with a low Signal to Noise ratio, the wind profiles were interpolated using Matlab's 'interp' function. This modification was most significant for the locations closest to the lidar, which experienced a time period with greater than 20 m/s speed. The model provided

output power profiles with slightly differing lengths, so Matlab's 'resample' function was used to align the samples from each profile and to use fewer points since the output was at a very high temporal resolution compared to the input wind speed profile.

Since the measured wind speeds were almost always greater than the rated speed of 11.4 m/s, the profiles were scaled down so that the relative energy content of the increases and decreases could be represented. Each velocity measurement was multiplied by a factor of 0.60.

Locations according to the streamlines from the radial velocity retrieval, marked in Figure 14, were selected for input to the wind turbine model to explore the correlation. The wind speed at all locations in the wind field can also be provided to the model such that the extractable energy content throughout the region at each time step can be plotted and tracked. Then a best fit can be done between the energy content at locations across which structures are seen advecting to provide the predicted energy at the downstream location.

The profile for the location nearest the lidar, the 'downstream' location, is shown in Figure 17. The high peak at about 500 minutes reaches the rated wind speed of the turbine so that even if the measurements greater than 20 m/s had been included, the energy content would be the same, unless the profile was scaled down further. The power output from the model maintains a profile that has the same trends as the wind speed profile. The output is much smoother and the substantial amount of noise in the wind speed profile is diminished.

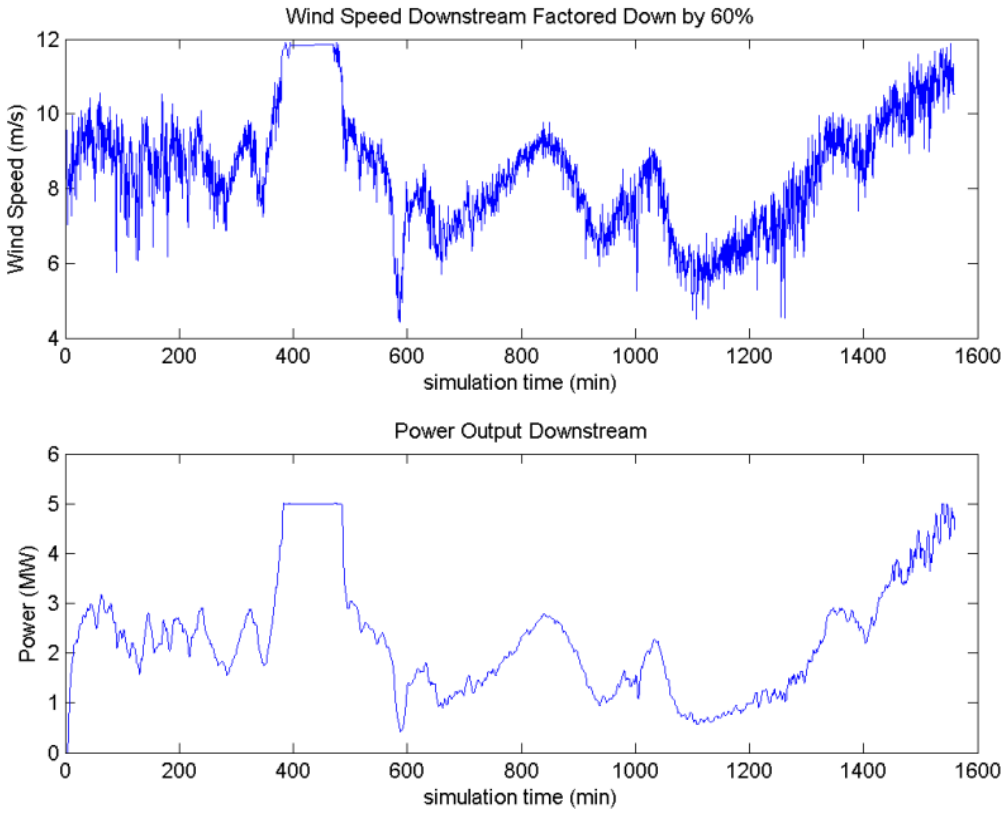

Figure 17. Wind speed input to model for "downstream" location, nearest the lidar (top) and the power output determined by the model (bottom). The wind speed profile was scaled down to 60% of the original speed to show the relative changes in energy content.

Dips and peaks in the wind speed can also be seen as changes in the energy content. This is shown on a smaller time scale in Figure 18.

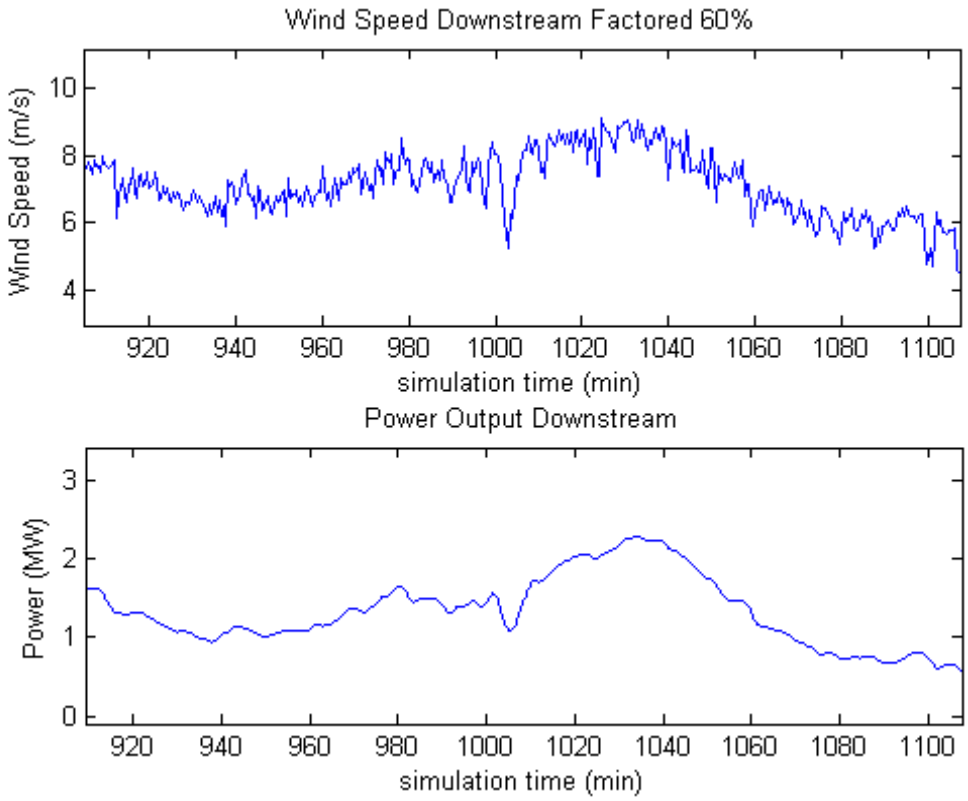

Figure 18. Short time period of the wind speed and energy content profiles at the downstream location.

Figure 19 demonstrates the similarity between the energy content at the downstream location and at Location 2, which is the second location from the downstream and 1340 meters upstream. Figure 20 also shows the similarity between the profiles at the different locations as well as the relative magnitudes and time of peaks. Other than the meteorological event that occurred between 05:00 and 08:00, the furthest upstream location in Figure 20 (top), Location 4 NW, has the highest magnitude and experiences the high and low peaks first, and further downstream locations have consecutively lower magnitudes and later peaks.

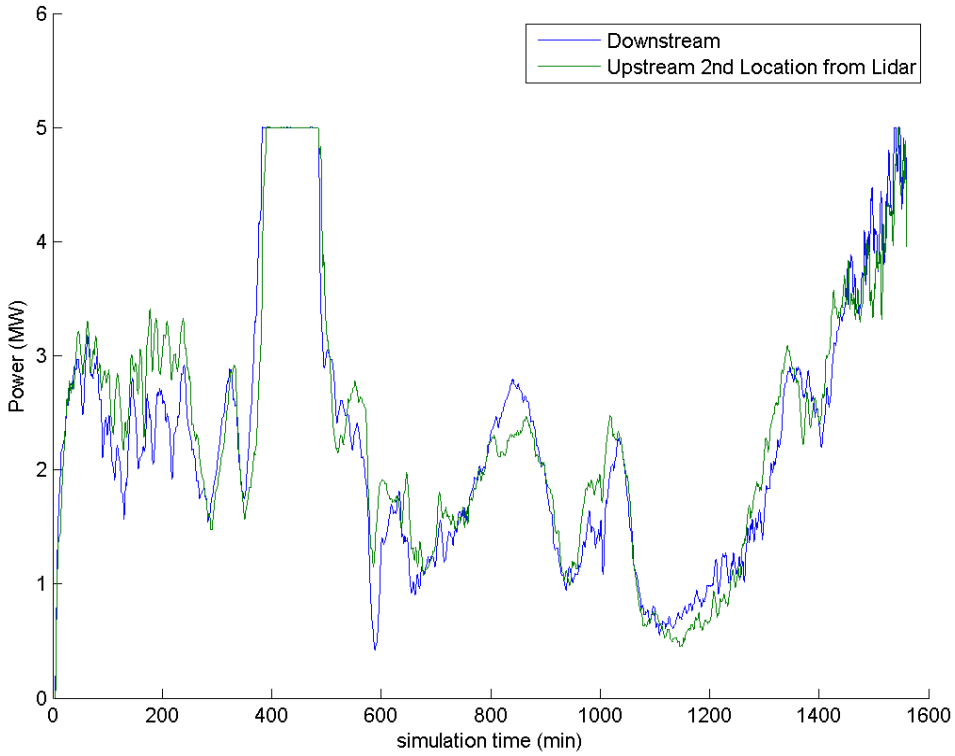

Figure 19. Energy content of the downstream location, near the lidar, and the upstream location that is second from downstream. The locations are 1340 meters apart. The wind speed profiles were scaled down to 60% of the original speed.

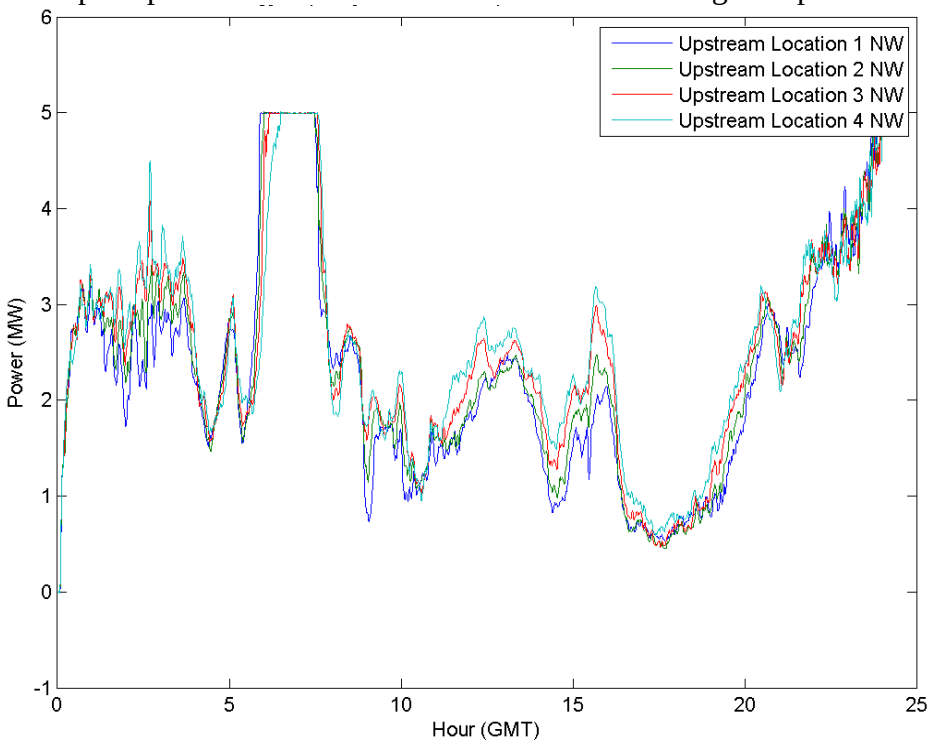

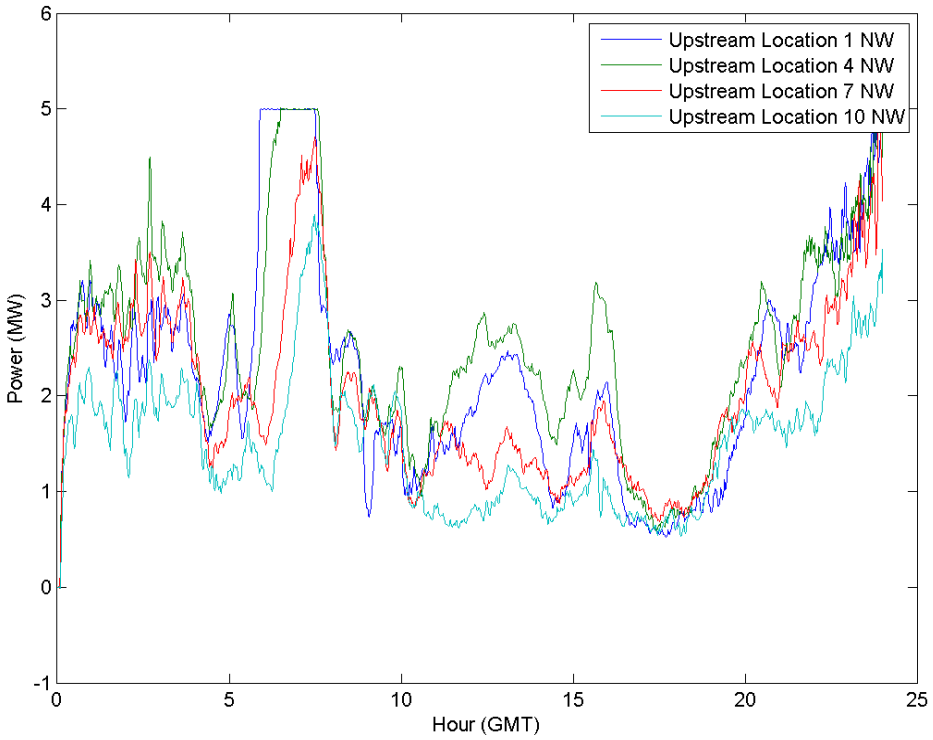

Figure 20. Energy content of the upstream locations, where Location 1 is closest to the downstream location. Each consecutive location is 670 meters further upstream. The wind speed profiles were scaled down to 60% of the original speed. Locations 1 through 4 (top) and selected Locations 1, 4, 7, and 10 (bottom).

The locations are each separated by 670 meters and very similar profiles are determined. With a high temporal measurement of the region, advection of structures that change the energy content available to the wind farm can be tracked and power predictions can be made.

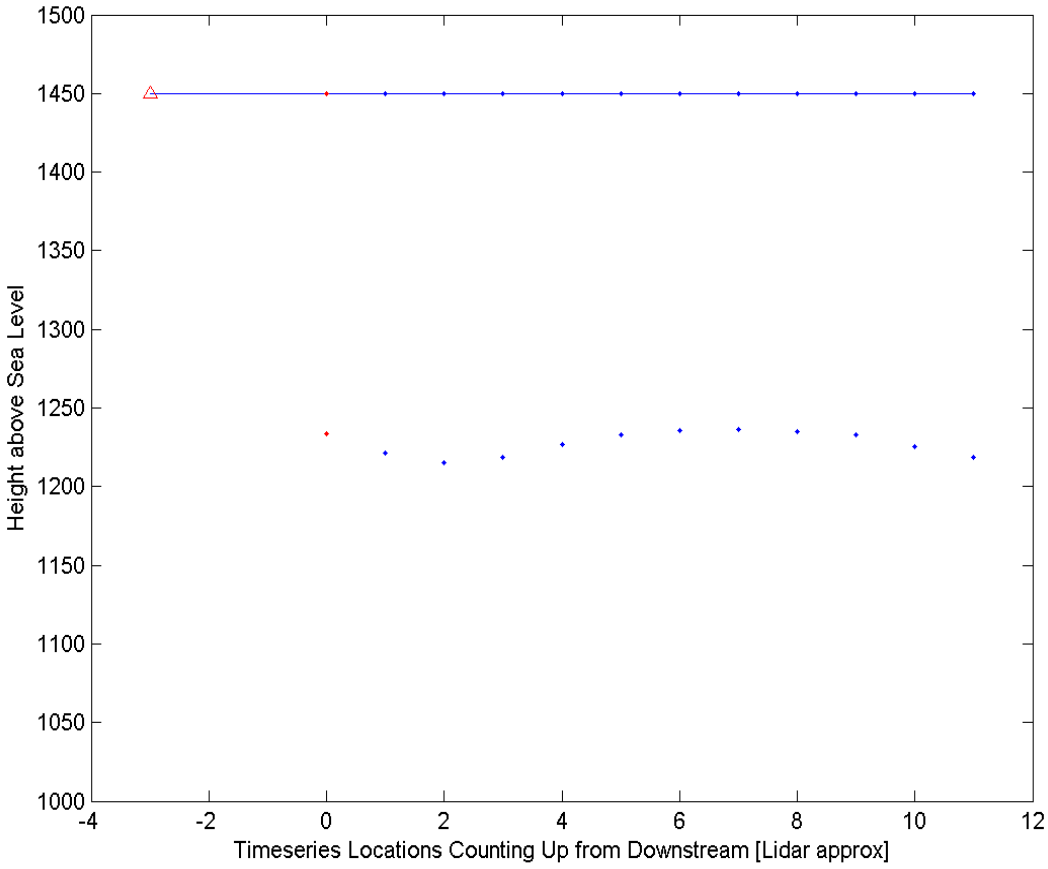

Figure 21. Height above sea level (meters) of the topography in Tehachapi at the location of the lidar (red triangle, located on the ground), the downstream location (red marker), and each upstream location (blue markers, numbered). The blue beam shows the height of the lidar measurements made at each location. The location of the lidar in the horizontal direction is not to scale.

The different magnitudes seen at each location in Figure 20 (bottom) result from both the momentum losses due to the earth's surface as well as funneling over the different heights of the terrain, shown in Figure 21, as described by Brower (2012, p. 2-4). The profiles presented in Figure 20 are based on the radial velocity measurements under the assumption that the wind is approximately in the radial direction, and further analysis of the magnitude relationship at locations with different terrain heights could be determined

after retrieval of the lidar data. The changes in relative magnitudes contribute to difficulty in correlating between these selected locations.

To make the prediction of energy content from upstream measurements, a correlation needs to be made between the wind farm location and the upstream location energy content profiles. First, the time shift, τ, between the profiles needs to be calculated according to Equation 2 based on the distance to the upstream location and the mean wind speed. This time shift could be made more accurate by an application of Euler's Method to incrementally update the time shift according to changes in wind speed along the streamline (Press et. al 1992). For events coming from other directions, such as the large peak at about 08:00 that was created by a meteorological event that did not advect along the direction of the mean wind, the propagation speed of those events as they move between locations can be used to predict their impact at the wind farm.

The upstream energy content time series should be truncated and shifted in time to align with that of the downstream profile. An example of the time shift after truncation is shown in Figure 22, from the downstream location and the ninth location upstream.

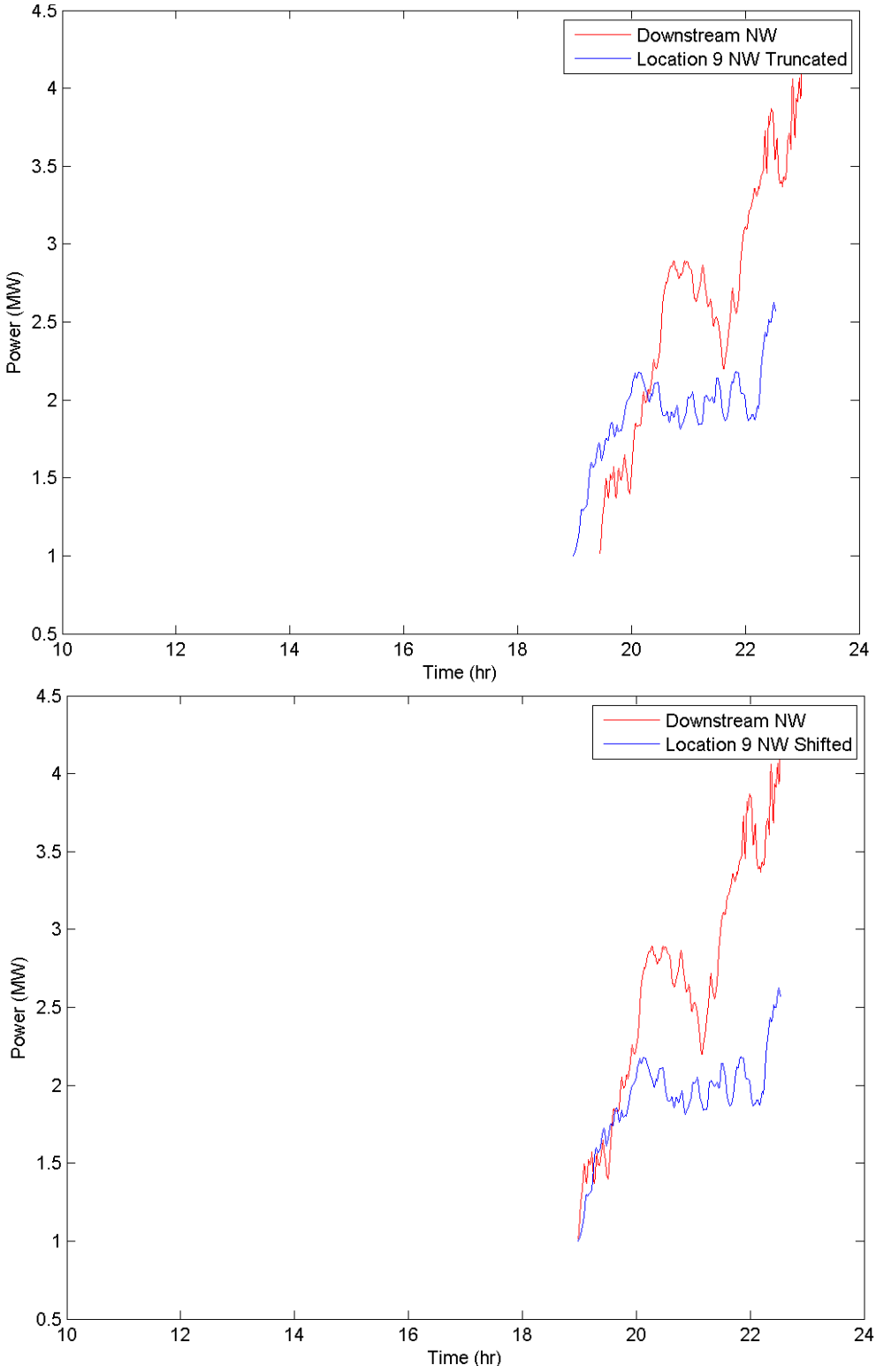

Figure 22. (Top) Truncated and (bottom) time shifted energy content profiles.

After shifting the upstream profile later in time by the determined time shift, a fit between the energy content profiles must be made. For this experiment, the fits that were tested were a linear fit, and a second, third, and fourth order polynomial fit. The given best fit can be used as a function to modify the energy content output by the 'virtual wind farm' at the upstream location to create a prediction for the following time period.

5.3 Prediction Accuracy

The predictions need to be evaluated according to standard metrics. A demonstration of how a prediction could look is shown in Figure 23 for analysis.

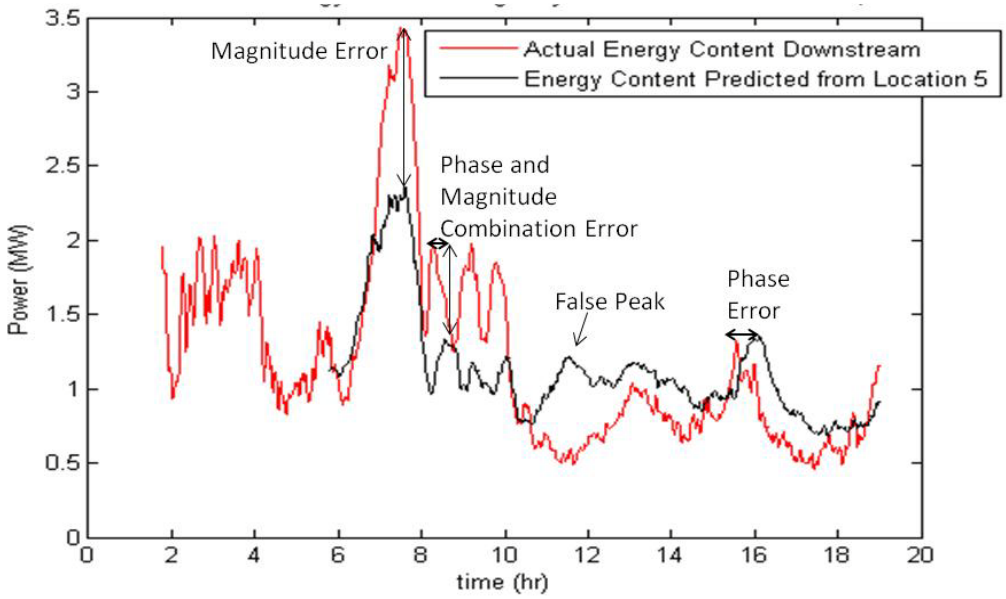

Figure 23. Example prediction plot

Two types of errors are defined for predicted peaks: phase and magnitude error (Ferreira et. al, 2010). The example prediction plot in Figure 23 gives examples of each. While the peak experienced at about 16:00 hours has approximately the same magnitude, the prediction peaks after the actual measured peak, an example of a phase error since the

prediction is not correct in time. On the other hand, the predicted peak at about 13:00 hours occurs at the correct time but has an incorrect magnitude. A 'false positive' occurs when a peak is predicted but does not occur, as shown just before 12:00 hours (Ferreira et. al, 2010).

The prediction was made for a time shift based on the average advection speed, approximated as 14 m/s. The energy content profiles at the upstream Location 3 and at the downstream location near the wind farm, 2010 meters apart, are displayed in Figure 24. The results of the predictions for various fit functions are given in Figure 25.

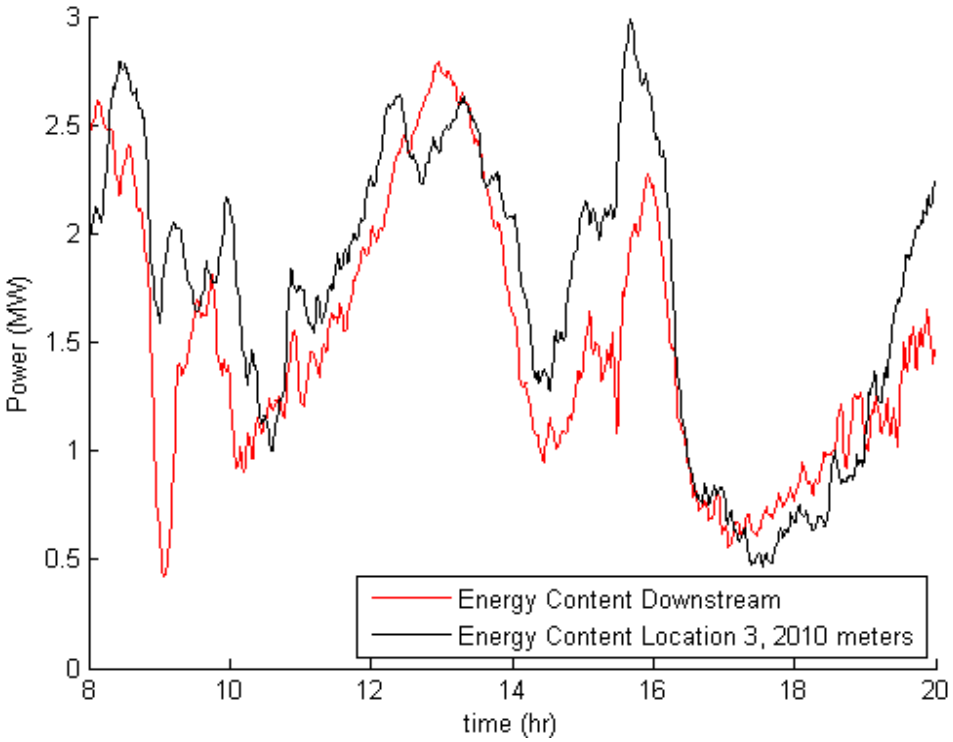

Figure 24. Energy content profiles at the upstream Location 3 and at the downstream location near the wind farm, 2010 meters apart.

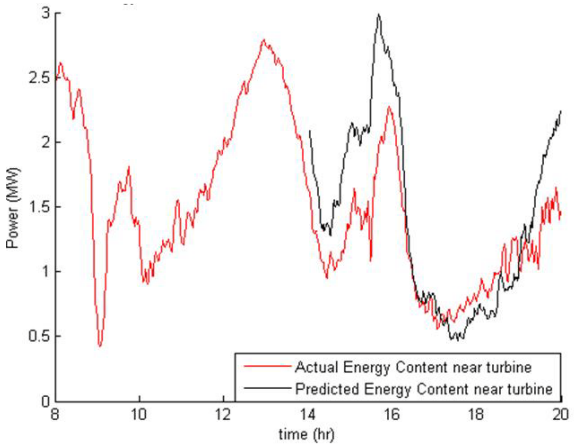

(a) Prediction is the measured value at Location 3, 2 km upstream, in real-time.

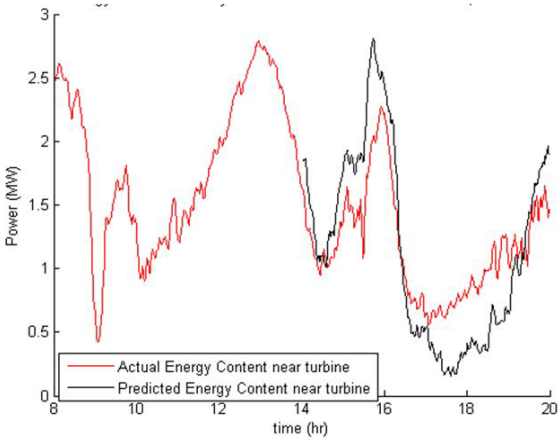

(c) Prediction is from Location 3, 2 km upstream, with a 3-minute time shift and 1st Order Polynomial fit from training period between 08:00 and 14:00. R^2=0.59.

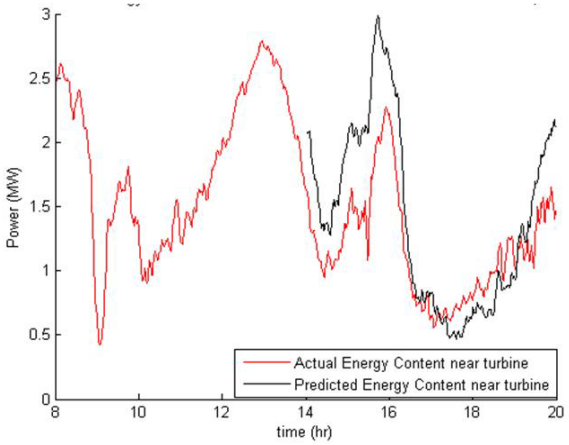

(b) Prediction is the measured value at Location 3, 2 km upstream, with a 3-minute time shift.

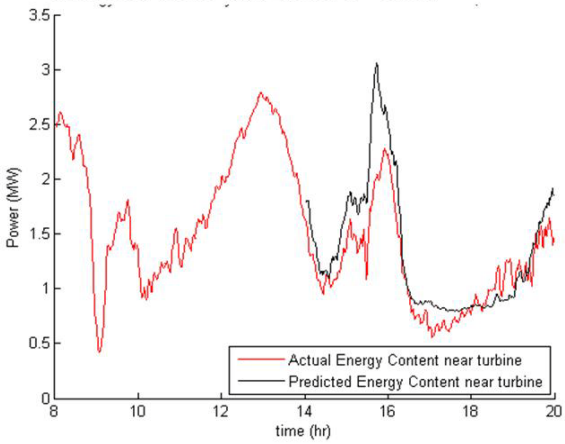

(d) Prediction is from Location 3, 2 km upstream, with a 3-minute time shift and 2nd Order Polynomial fit from training period between 08:00 and 14:00. R^2=0.60.

Figure 25. Predictions of energy content at the downstream location using various fit functions with the energy content at Location 3, 2010 meters upstream.

Figure 25a shows the energy content at Location 3 upstream as the prediction, with no time shift. This represents the actual measured energy content profiles at Location 3, given as the prediction, and at the downstream location near the wind turbine in real-time. In Figure 25b, this profile is shifted by 3 minutes, according to the advection speed of 14

m/s and distance between the locations, 2010 meters. For this small time shift, the profile does not show a very noticeable change, and any improved alignment of small peaks is difficult to identify. The first order polynomial fit is applied to the time-shifted upstream profile to create the prediction shown in Figure 25c. The first order fit is determined by calculating the best correlation between the energy content profiles during a training period of historic data for the time period before the prediction is started. In this case, the training period was six hours long from 08:00 to 14:00 and the prediction is started at 14:00. That function is then applied to the upstream profile to create the prediction. The magnitude between about 14:00 and 16:00 is improved, but the magnitude for the downward peak around 18:00 is worsened. This implies that the fit, which is based on the training period from just before the start of the prediction, decreases in validity as time progresses, likely because of changes in the meteorological conditions. It is expected that a continually updated fit would improve this result. Figure 25d shows the prediction according to a second order polynomial fit. While the peak at 16:00 has a larger magnitude error, the rest of the signal has an improved magnitude and gives the best prediction.

The prediction using the first order polynomial fit but a shorter training period is shown in Figure 26.

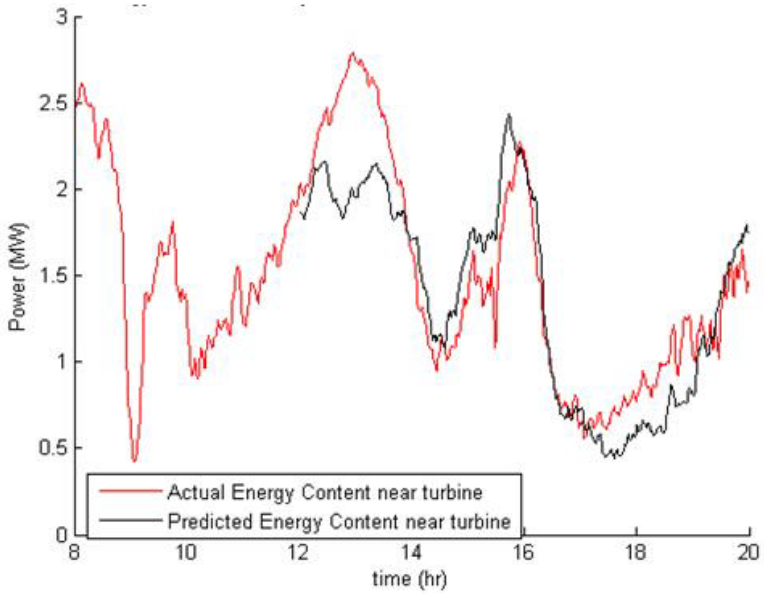

Figure 26. Prediction of energy content at the downstream location with the energy content at Location 3, 2010 meters upstream, using 1st Order Polynomial from training period between 08:00 to 12:00. R^2=0.42.

This prediction used a 4-hour training period, from 08:00 to 12:00. The magnitude of this prediction is better than the first order fit from a longer training period which is because the misshaped peak at 13:00 was not part of the training period. The R^2correlation value is lower because less information was used for the training.

The Mean Absolute Error (MAE) and the standard deviation of the absolute error (Std) are commonly used metrics for predictions in the wind industry (Ferreira et. al, 2010). MAE and Std were calculated for each of the predictions compared to the actual energy content.

$$AE(t) = |\hat{y}(t) - y(t)| \tag{14}$$

$$MAE = \frac{\sum_{t=1}^{N} AE(t)}{N} \tag{15}$$

$$Std = \sqrt{\frac{\sum_{t=1}^{N}(AE(t) - MAE)}{N-1}} \tag{16}$$

AE is the Absolute Error between the prediction, $\hat{y}(t)$, and the observed value, $y(t)$, at a given time, t. N is the number of points in the prediction. Lower MAE and Std values signify better predictions.

The MAE is plotted for the linear and second order polynomial fit for both the 4 and 6-hour training periods in Figure 27. The linear fit with the 4 hour training gave the prediction with the lowest error for most of the upstream locations. The second order fit with the 6-hour training has slightly better performance for several locations, as was seen in the results shown in Figure 25. For all the locations further upstream than Locations 6, the 6-hour training did not perform as well as the 4-hour training. The different relative magnitudes that were captured in the longer training period caused difficulty in performing a successful correlation, resulting in high error in the predictions for these cases. In Figure 28 the MAE is shown for a prediction made based on the real-time upstream energy content, the time-shifted upstream energy content according to advection at 14 m/s, and the linear and second order polynomial fit correlations, after the time shift, using the 4-hour training period. The time shift alone has a small effect on the error compared to the prediction using the real-time upstream measurements. The polynomial fits actually do not improve the prediction for the closest two locations and for Locations 6 and 7. The relative magnitudes with the downstream energy content were not well-established by the correlation for these locations.

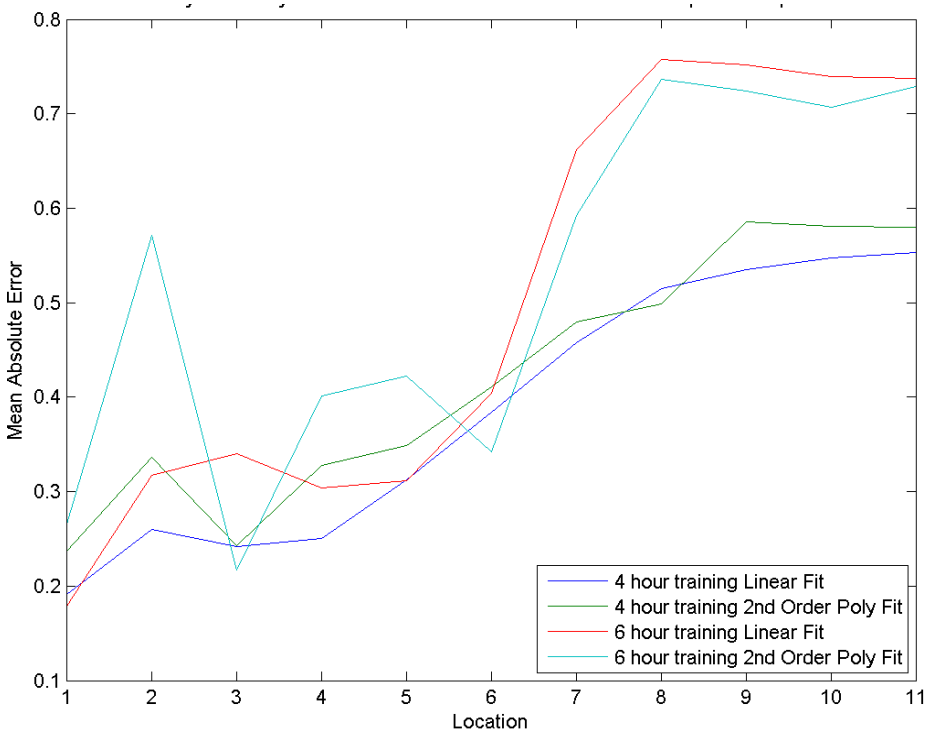

Figure 27. MAE for the linear and 2nd order polynomial fit for both the 4 and 6-hour training periods for the prediction result from time-shifted energy content according to advection at approximate wind speed.

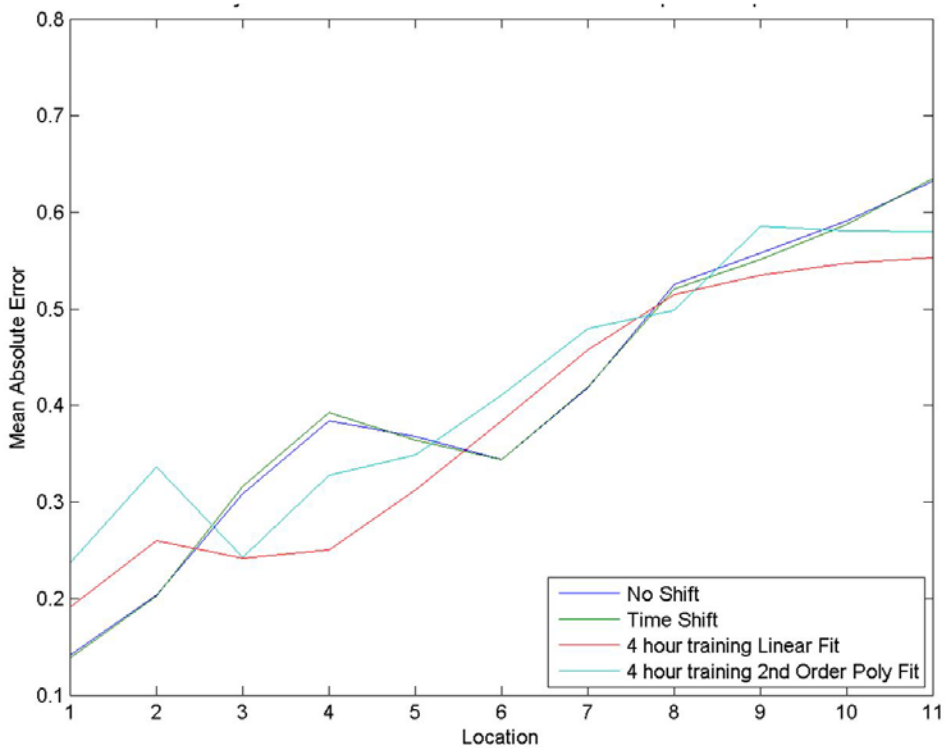

Figure 28. MAE for upstream energy content without any time shift, the time-shifted upstream energy content according to advection at 14 m/s, and the linear and second order polynomial fit correlations, after the time shift, using the 4-hour training period.

While it was expected that the relationship between wind speed profiles would be linear as speed would change due to momentum loss at the surface and, according to a factor calculated by the Law of the Wall, for different heights above ground level, the energy content in fact relates the cube of the wind speed and likely requires a higher-order fit to relate the profiles for that reason as well as due to the more complex effects of the terrain. The prediction and error statistics using third and fourth order polynomial fits are shown in Figure 29.

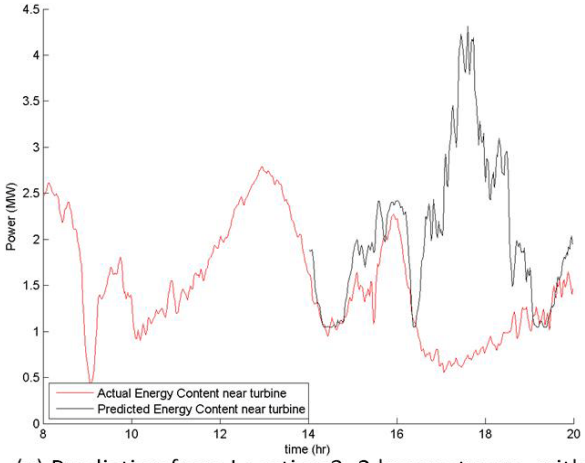

(a) Prediction from Location 3, 2 km upstream, with a 3-minute time shift and 3rd Order Polynomial fit from training period between 08:00 and 14:00.

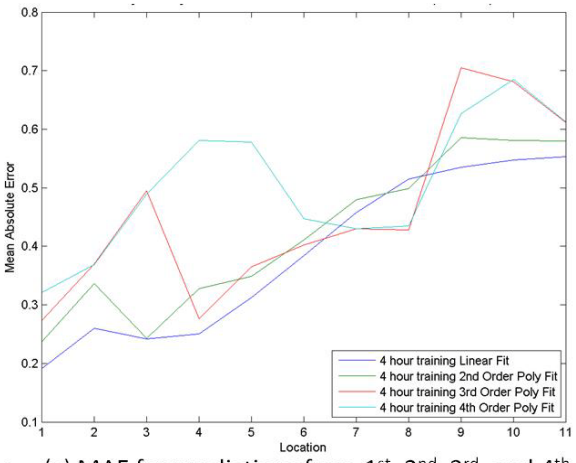

(c) MAE for predictions from 1st, 2nd, 3rd, and 4th order polynomial fit correlations of Location 3, using time shift and 4-hour training period.

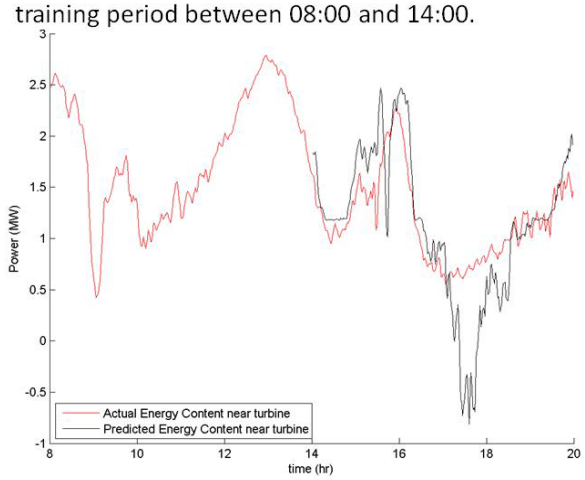

(b) Prediction from Location 3, 2 km upstream, with a 3-minute time shift and 4th Order Polynomial fit from training period between 08:00 and 14:00.

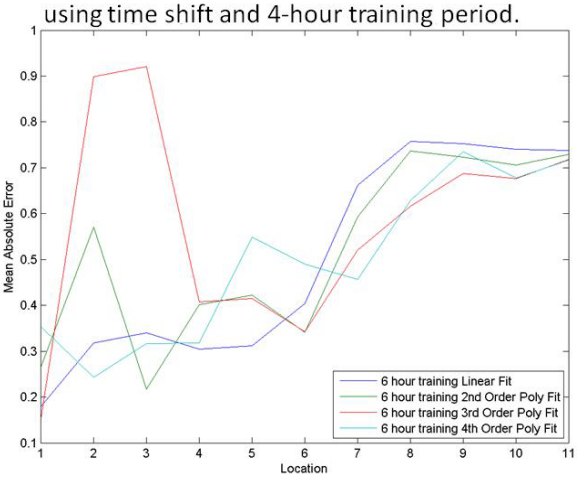

(d) MAE for predictions from 1st, 2nd, 3rd, and 4th order polynomial fit correlations of Location 3, using time shift and 6-hour training period.

Figure 29. Predictions of energy content at the downstream location using (a) 3rd order and (b) 4th order polynomial fit functions with the energy content at Location 3, 2010 meters upstream. MAE statistics for predictions according to location upstream for (c) 4-hour and (d) 6-hour training time periods.

The magnitude is better captured by the third and fourth order polynomial fits except at the local minima in energy content just before 18:00, as the conditions have changed from the training period conditions by that time. The linear fit still has the best performance for the 4-hour training period, but does not have as good performance as the

4^{th} order polynomial fit for many of the locations when the 6-hour training period is used. The predictions with an MAE of greater than 0.4, the predictions were not considered successful. For the furthest upstream locations, none of the fits give successful predictions.

A more complex correlation, such as the correlation generated by training an Artificial Neural Network model, is expected to provide a better prediction. An Artificial Neural Network could also make use of the spatially dense and extensive measurements made by the lidar, such that measurements at more than one location can be input to make the prediction. For correlations according to energy profiles at a single upstream location, the location could be selected to more closely follow the streamlines and use retrieved wind speed and direction from a validated retrieval technique. The location also could be selected according to the upstream energy content profile that gives the best correlation during each training period. Training could be done over a long period of time that averages out the misaligned peaks and could be updated as wind conditions change. Testing the predictions over a longer time period, and in the context of the surrounding meteorological conditions, would provide information for conditions under which the correlation method is most valid.

5.4 Ramp Detection

A change in the extractable energy content of the wind compared to the previous average is called a ramp. Differing definitions are used to evaluate ramps (Ferreira et. al, 2010). To identify ramps for this study, a change in power output by 25% of the turbine power capacity, compared to the average for the previous hour, was applied. A positive

ramp is defined as an increase by 25% and a negative ramp as a decrease by 25% of the power capacity. The change in power output, P' at a time t, is calculated from the difference between the power output, P(t), and the mean of the previous time period by,

$$N = \frac{T}{\Delta t} + 1 \tag{17}$$

$$P'(t) = P(t) - \frac{\sum_{n=0}^{N-1} P(t - n\Delta t)}{N} \tag{18}$$

where N is the number of samples in the time period, T, which in this case is one hour, and Δt is the time step between sampled measurements. A ramp event, shown in Figure 30, was detected by the lidar. The ramp event propagated from the southeast, counter to the direction from which the wind advects, reaching Location 11 last.

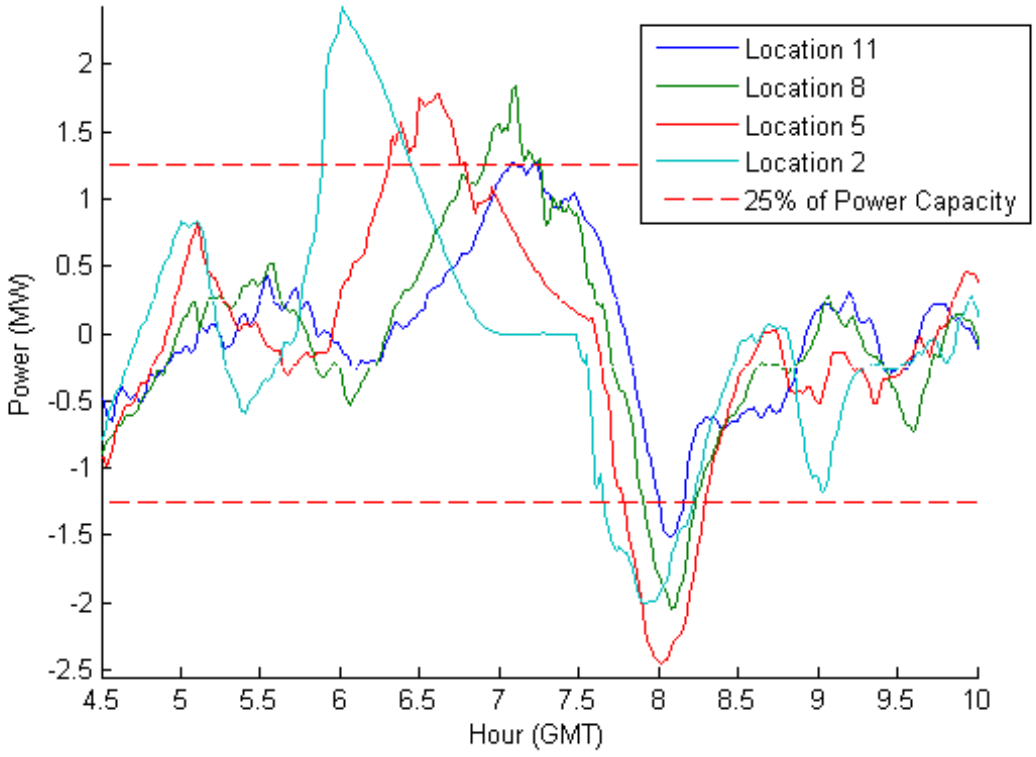

Figure 30. Ramps of 25% of turbine power capacity, June 27 GMT. Each of the presented locations are 2.25 km apart.

The positive ramp can be detected at Location 2, 6.75 km ahead, and can be seen occurring subsequently at the further locations. At Location 2, this ramp is recognized before 06:00 GMT. It occurs closer to the wind farm, at Location 11, after 07:00 GMT, giving over an hour of advance notice of the oncoming ramp event. The negative ramp, just before 08:00 GMT, also occurs subsequently at locations further downstream. The time between peaks at each location is smaller than for the positive ramp. The speed of propagation must be considered, as described for the correlation studies of advection, to predict the time of arrival of the ramp at the wind farm.

This ramp is barely noticeable when the full extractable energy content is assumed, rather than scaled to 60% of the energy content, since the wind speeds barely drop below the turbine's rated value. However, correlating the energy content without this limit makes it possible to account for the decrease in magnitude of wind speeds between upstream and downstream that could cause a decrease below rated power at the downstream location.

In Figure 31, the radial velocity is plotted for several sweeps 30 minutes apart. The data was limited to 20 m/s and any higher values were removed. The interface between velocity at 20 m/s and missing data where the velocity was higher can be seen moving through the domain.

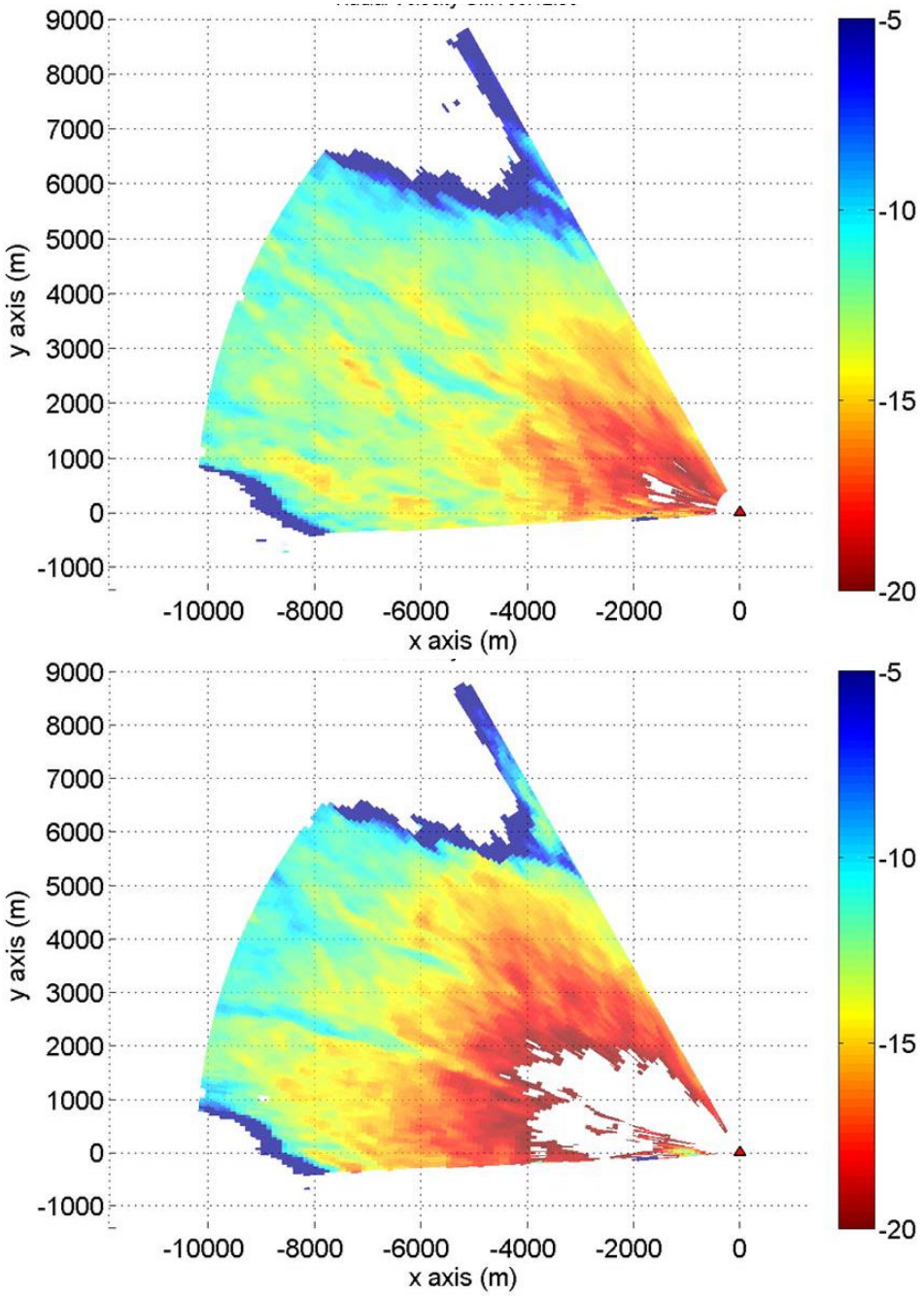
9000
8000
7000
6000
5000
4000
3000
2000
1000
0
-1000
y axis (m)
-10000
-8000
-6000
-4000
-2000
0
x axis (m)
-5
-10
-15
-20

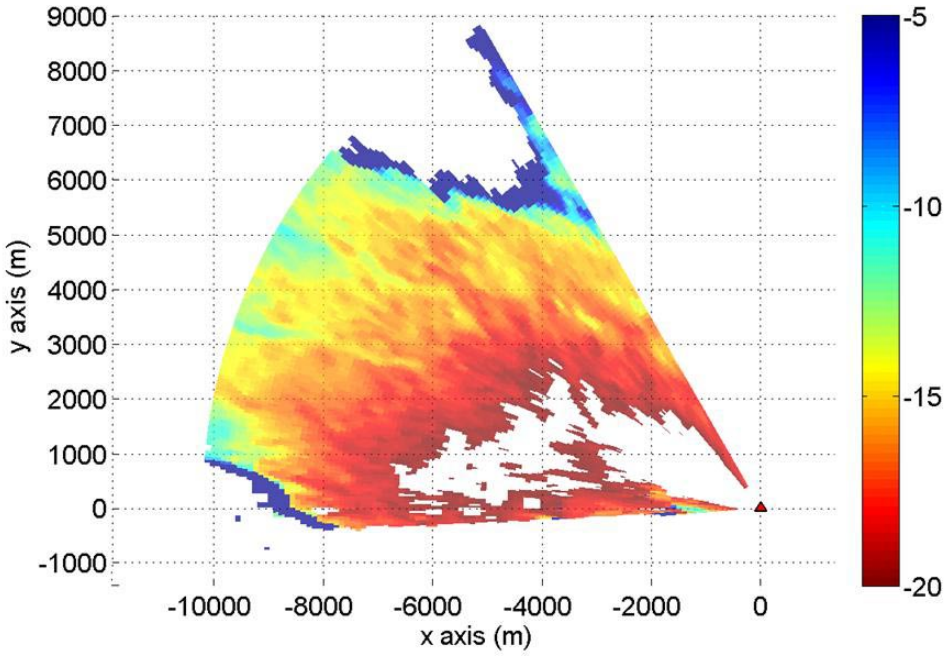

Figure 31. Propagation of the ramp event where radial velocities greater than 20 m/s are shown as missing data. First image is at GMT 06:03 on June 27, with about 30 minutes between each following image. The colorbar is in m/s and positive values represent movement away from the lidar along its line of sight.

Visual inspection of the plots also makes it possible to recognize this ramp event and track its movement.

The ramp is expected to be a meteorological event due to a propagating front creating a depression in the height of the inversion capping layer, causing an increase in wind speed as winds are funneled through a narrower volume between the terrain and the capping layer. Since the ramp event moved opposite the direction of advection, wind farm operators must monitor changes in energy content from all directions to capture all ramp events. The height of the terrain (Brower, 2012, p. 2-4) and the direction of the ramp event's propagation will affect the magnitude of the change in the energy content at locations along streamlines.

This result shows that ramps can be detected as they propagate by monitoring the change of the extractable energy content from the running average over the selected time period. A lidar makes it possible to measure the winds over a large spatial region with high accuracy and temporal resolution and effectively predict large ramp events.

Chapter 6

CONCLUSIONS

This study provided an example of a correlation analysis to make predictions of wind power output based on velocity measurements upstream of a wind farm using a "Virtual wind farm" concept, presented a value quantifying turbulence intensity and tracking movement of turbulent regions, and gave an example of identifying propagation of a ramp event. This study showed that there is clearly a relationship between the energy content measured with time by the Doppler lidar at the different locations.

The assumption of advection along a radial direction from the lidar provided a reasonable fit between energy content at upstream and downstream locations, making a prediction possible. An improved selection of locations could be made after retrievals of the decomposed velocity so that wind speed and direction at all measured locations are available. Streamlines can be followed upstream from a wind farm location to determine a location from which wind structures are expected to advect. A sector VAD approach was applied to show that streamlines remained consistent over a 20-minute period and did follow a radial direction near the center of the sweep, supporting the choice of upstream locations for this study. To determine the streamlines for future projects, retrieval techniques such as Volume Velocity Processing should be evaluated for applicability in complex terrain. Experimentation should include *in situ* measurements within or near the region of the lidar's scans for validation.

Some additional work should be performed studying the use of VVP in complex topography to consider whether smaller sector sizes are valid. For application of the VVP

method, the lidar scanning pattern should include sweeps of at least two different elevation angles to provide a volume for processing. If only one sweep can be made, it should be at zero-degree elevation to remove components of vertical velocity from the measurements. The sweeps should be repeating rather than back and forth and should view the same location with a small enough time interval to track advection at the speed of expected prevailing winds.

A formulation of the turbulence intensity is defined spatially, relating time of advection to the size of eddies. Termed spatial variance, it is calculated by the variation from the mean along the streamline in the downstream direction over a distance related to the speed of advection and time scale of interest. With this formulation, regions of increased turbulence can be tracked as they advect. This makes it possible to provide advance information of intensity and length of turbulent patches to wind farm operators who can apply pitch controls to their turbines to harness the additional energy or minimize loading due to the turbulence.

Energy content was determined from the radial velocity measurements at locations along a streamline parallel to the radial direction using a Simulink model of the NREL 5MW turbine. The energy content was capped for wind speeds above the turbine's rated speed. However, correlating the energy content without this capping, for example by decreasing the wind speed profile by a constant factor, makes it possible to account for the decrease in magnitude of wind speeds between upstream and downstream that could cause a decrease below rated power at the downstream location.

The phase and magnitude errors in the predictions could result from the points not actually being along a streamline and therefore not actually experiencing the same structures. The locations were chosen based on advection of small-scale structures approximately along streamlines from historical data. The time shift was calculated according to the speed of advection and the distance between the locations. For more precision, the time shift should be updated from the velocity of the wind speed over the streamline in real-time.

The prediction was calculated from a best fit between locations over a training period of historical data. For this study, it was found that the linear fit, which relates the magnitude and the rate of change of the wind velocities, worked best, and the longer training time period also decreased the error. Making this fit for a longer training period or updating it for the latest historical data would improve the correlation. Since magnitude errors were seen even from the linear fit, it is also recommended that additional fit types could be evaluated.

A straightforward correlation method was applied in this study to present the ability of lidar measurements to inform short-term power predictions by tracking advection of energy content in wind structures. With this shown, it is suggested that future work should explore the advectability of structures across larger distances upstream of wind farms. The lidar can be located ahead of wind farms, when the upstream direction is known, and make measurements of structures moving toward the wind farm further in advance. For lidars that are located so far upstream that they cannot measure energy content at the wind farm, correlations of energy content can be done

using *in situ* measurements at the wind farm or the power generated by the turbines. Applying the results to real practice would assist in evaluating this method. It is important to evaluate this prediction method using real data from wind turbines to include effects that are not sufficiently addressed by the turbine model, such as yaw effects, vertical wind gradients over the turbine rotor, and turbulence, which can be measured by the lidar at the turbine and upstream (Wagner, 2009).

Opportunities are available to expand on the correlation method using historical data between two locations that was presented in this study. Recommended next steps are using the lidar data with terrain data as input to a NWP model or generalizing the correlation to a neural network with learning and adaptability in addition to the capacity for multiple inputs which the lidar is highly capable of providing (Sheela and Deepa, 2013; Bilgili, Sahin, & Yasar, 2007). Since no papers were found that applied lidar measurement data to neural network methods for wind power prediction, this is a new route that can be taken for future expansion of this project. The prediction can be made for a wind farm by expanding the turbine model into a model of a full wind farm, which also makes it possible to determine control schemes according to wake effects.

REFERENCES

Adams, A. (2014). Taking the power out of the wind: the relationship between wind energy and the atmosphere. Arizona State University Mechanical and Aerospace Engineering Seminar Series, Tempe, AZ.

Ágústsson, H., & Ólafsson, H. (2009). Forecasting wind gusts in complex terrain. Meteorology and Atmospheric Physics, 103(1-4), 173-185. doi:10.1007/s00703-008-0347-y

Alexiadis, M. C., Dokopoulos, P. S., & Sahsamanoglou, H. S. (1999). Wind speed and power forecasting based on spatial correlation models. Energy Conversion, IEEE Transactions on, 14(3), 836-842. doi:10.1109/60.790962

Aitken, M. (2014). Utility-scale wind turbine wake characterization using nacelle-based long-range scanning lidar. Journal of Atmospheric and Oceanic Technology, 31(7), 1529.

Atkins, N. (2001). Turbulence Intensity and Turbulent Kinetic Energy (TKE) [Course content]. Lyndon State College. Retrieved from http://apollo.lsc.vsc.edu/classes/met455/notes/section3/3.html.

Atkins, N. (2007). Turbulence and Taylors Hypothesis [Course content]. Lyndon State College. Retrieved from http://apollo.lsc.vsc.edu/classes/met455/notes/section2/2.html.

Bechrakis, D. A., & Sparis, P. D. (2004). Correlation of wind speed between neighboring measuring stations. *Energy Conversion, IEEE Transactions on, 19*(2), 400-406. doi:10.1109/TEC.2004.827040

Betz, A. (1966) Introduction to the Theory of Flow Machines. (D. G. Randall, Trans.) Oxford: Pergamon Press.

Bilgili, M., Sahin, B., & Yasar, A. (2007). Application of artificial neural networks for the wind speed prediction of target station using reference stations data. *Renewable Energy*,*32*(14), 2350-2360. doi:http://dx.doi.org.ezproxy1.lib.asu.edu/10.1016/j.renene.2006.12.001

Boccippio, D. (1995). A diagnostic-analysis of the VVP single-Doppler retrieval technique. Journal of Atmospheric and Oceanic Technology, 12(2), 230-248.

Bossanyi, E. (2013). Un-freezing the turbulence: Application to LiDAR-assisted wind turbine control. *Renewable Power Generation, IET, 7*(4), 321-329. doi:10.1049/iet-rpg.2012.0260

Brower, Michael. (2012). Wind Resource Assessment. Wiley. Retrieved from <http://www.myilibrary.com?ID=362201>

Carpenter, R. L., Shaw, B. L., Margulis, M., Barr, K. S., Baynard, T., Yates, D., Sharp, J. (2013). Short-term numerical forecasts using WindTracer lidar data. American Meteorological Society: Fourth Conference on Weather, Climate, and the New Energy Economy, Austin, TX.

Choukulkar, A. (2013). Coherent Doppler LIDAR for boundary layer studies and wind energy

Choukulkar, A., Calhoun, R., Billings, B., & Doyle, J. (2012). Investigation of a complex nocturnal flow in Owens Valley, California using coherent Doppler lidar. Boundary-Layer Meteorology, 144(3), 359-378. doi:http://dx.doi.org.ezproxy1.lib.asu.edu/10.1007/s10546-012-9729-2

Deshpande, A. S., & Peters, R. R. (2012). Wind turbine controller design considerations for improved wind farm level curtailment tracking. *Power and Energy Society General Meeting, 2012 IEEE,* 1-6. doi:10.1109/PESGM.2012.6343975

Drew, D. R., Barlow, J. F., & Lane, S. E. (2013). Observations of wind speed profiles over greater London, UK, using a Doppler lidar. *Journal of Wind Engineering and Industrial Aerodynamics, 121*(0), 98-105. doi:http://dx.doi.org.ezproxy1.lib.asu.edu/10.1016/j.jweia.2013.07.019

El Kasmi, A., & Masson, C. (2010). Turbulence modeling of atmospheric boundary layer flow over complex terrain: A comparison of models at wind tunnel and full scale. *Wind Energy,13*(8), 689-704. doi:10.1002/we.390

Ferreira, C., Gama, J., Matias, L., Botterud, A., & Wang, J. (2011). (Decision and Information Sciences), (INESC Porto). A survey on wind power ramp forecasting. Retrieved from http://www.osti.gov/scitech/servlets/purl/1008309

Frehlich, R., & Kelley, N. (2008). Measurements of wind and turbulence profiles with scanning Doppler lidar for wind energy applications. Selected Topics in Applied Earth Observations and Remote Sensing, IEEE Journal of, 1(1), 42-47. doi:10.1109/JSTARS.2008.2001758

Frehlich, R. (2001). Estimation of velocity error for Doppler lidar measurements. Journal of Atmospheric and Oceanic Technology, 18(10), 1628.

Frehlich, R. (2013). Scanning doppler lidar for input into short-term wind power forecasts. Journal of Atmospheric and Oceanic Technology, 30(2), 230.

Greaves, B., Collins, J., Parkes, J., & Tindal, A. (2009). Temporal forecast uncertainty for ramp events. Wind Engineering, 33(4), 309-319. doi:http://dx.doi.org.ezproxy1.lib.asu.edu/10.1260/030952409789685681

Hirth, B. D., Schroeder, J. L., Gunter, W. S., & Guynes, J. G. (2014). Coupling doppler radar-derived wind maps with operational turbine data to document wind farm complex flows. Wind Energy. doi:10.1002/we.1701

Hutton, D. (2008). WindTracer WTX System Operation User Manual: Lockheed Martin Coherent Technologies.

Jiménez, P. (2013). On the ability of the WRF model to reproduce the surface wind direction over complex terrain. *Journal of Applied Meteorology and Climatology, 52*(7), 1610.

Jonkman, J., Butterfield, S., Musial, W., Scott, G. (2007). Definition of a 5-MW reference wind turbine for offshore system development. NREL/TP-500-38060. National Renewable Energy Laboratory, Golden, CO.

Krishnamurthy, R. (2010). Large-eddy simulation-based retrieval of dissipation from coherent Doppler lidar data. *Boundary-Layer Meteorology, 136*(1), 45.

Krishnamurthy, R. (2013). Wind farm characterization and control using coherent Doppler lidar. (Ph.D., Arizona State University).

Krishnamurthy, R., Choukulkar, A., Calhoun, R., Fine, J., Oliver, A., & Barr, K. S. (2013). Coherent Doppler lidar for wind farm characterization. *Wind Energy, 16*(2), 189-206. doi:10.1002/we.539

Krishnamurthy, R., Calhoun, R., Billings, B., & Doyle, J. (2011). Wind turbulence estimates in a valley by coherent Doppler lidar. *Meteorological Applications, 18*(3), 361-371. doi:10.1002/met.263

Krishnamurthy, R., Calhoun, R., & Fernando, H. (2010). Large-eddy simulation-based retrieval of dissipation from coherent Doppler lidar data. Boundary-Layer

Meteorology, 136(1), 45-57. doi:http://dx.doi.org.ezproxy1.lib.asu.edu/10.1007/s10546-010-9495-y

Lange, M., & Focken, U. (2006). *Physical approach to short-term wind power prediction*. Berlin; New York: Springer.

Mann, J. (1998). Wind field simulation. *Probabilistic Engineering Mechanics, 13*(4), 269-282. doi:http://dx.doi.org.ezproxy1.lib.asu.edu/10.1016/S0266-8920(97)00036-2

METAR Information for KTSP. (n.d.). Retrieved October 22, 2014, from http://weather.gladstonefamily.net/site/KTSP

Na Wang, Johnson, K. E., & Wright, A. D. (2011). LIDAR-based FX-RLS feedforward control for wind turbine load mitigation. *American Control Conference (ACC), 2011*, 1910-1915.

Na Wang, Johnson, K. E., & Wright, A. D. (2013). Comparison of strategies for enhancing energy capture and reducing loads using LIDAR and feedforward control. *Control Systems Technology, IEEE Transactions on, 21*(4), 1129-1142. doi:10.1109/TCST.2013.2258670

NOAA National Climatic Data Center. (n.d.). [Data file]. Retrieved August 23, 2014, from http://www.ncdc.noaa.gov/cdo-web/datasets/GHCND/stations

NOAA's National Weather Service. (n.d.). Glossary - NOAA's National Weather Service. Retrieved October 10, 2014, from http://w1.weather.gov/glossary/

Parks, K., Wan, Y. H., Wiener, G., & Liu, Y. (2011). Wind Energy Forecasting: A Collaboration of the National Center for Atmospheric Research (NCAR) and Xcel Energy. doi:10.2172/1027161

Parish, T. R. (2000). Forcing of the summertime low-level jet along the California coast. *Journal of Applied Meteorology (1988), 39*(12), 2421; 2421-2433; 2433.

Pomeroy, K. R., & Parish, T. R. (2001). A case study of the interaction of the summertime coastal jet with the california topography. *Monthly Weather Review, 129*(3), 530.

Press, W. H.; Flannery, B. P.; Teukolsky, S. A.; and Vetterling, W. T. Numerical Recipes in FORTRAN: The Art of Scientific Computing, 2nd ed. Cambridge, England: Cambridge University Press, p. 710, 1992.

Sathe, A., & Mann, J. (2012). Measurement of turbulence spectra using scanning pulsed wind lidars. Journal of Geophysical Research.D. Atmospheres, 117(d1)

Šavli, M. (2012). Turbulence kinetic energy – TKE [Course content]. University of Ljubljana. Retrieved from http://mafija.fmf.uni-lj.si/seminar/files/2011_2012/MaticSavli_2.pdf

Schetz, J. A.*Boundary layer analysis* American Institute of Aeronautics and Astronautics.

Schlipf, D., Cheng, P. W., & Mann, J. (2013). Model of the correlation between lidar systems and wind turbines for lidar-assisted control. Journal of Atmospheric and Oceanic Technology, 30(10), 2233-2240. doi:http://dx.doi.org.ezproxy1.lib.asu.edu/10.1175/JTECH-D-13-00077.1

Sheela, K. G., & Deepa, S. N. (2013). A review on neural network models for wind speed prediction. *Wind Engineering, 37*(2), 111-124. doi:10.1260/0309-524X.37.2.111

Shrestha, G. M. (1974). Approximate method for solving boundary layer equations. *AIAA Journal, 12*(3), 382; 382-384; 384.

Smalikho, I. N., Banakh, V. A., Pichugina, Y. L., Brewer, W. A., Banta, R. M., Lundquist, J. K., & Kelley, N. D. (2013). Lidar investigation of atmosphere effect on a wind turbine wake.*Journal of Atmospheric & Oceanic Technology, 30*(11), 2554-2570. doi:10.1175/JTECH-D-12-00108.1

Treinish, L. A., Cipriani, J., Praino, A. P., Diaz, J., & Dorronsoro, J. R. (2013). Precision wind power forecasting via coupling of turbulent-scale atmospheric modelling with machine learning methods. American Meteorological Society: Fourth Conference on Weather, Climate, and the New Energy Economy, Austin, TX.

Verwaal, N. W., van der Veen, G. J., & van Wingerden, J. W. (2014). Predictive control of an experimental wind turbine using preview wind speed measurements. *Wind Energy*, , n/a-n/a. doi:10.1002/we.1702

Wagner, R. (2009). The influence of the wind speed profile on wind turbine performance measurements. *Wind Energy (Chichester, England), 12*(4), 348; 348-362; 362.

Wang, N. (2013). Lidar-assisted feedforward and feedback control design for wind turbine tower load mitigation and power capture enhancement. (Ph.D., Colorado School of Mines). *ProQuest Dissertations and Theses*. (1468723223).

Weitkamp, C. (2005). Lidar: Range-resolved optical remote sensing of the atmosphere. Springer Series in Optical Sciences, Volume 102. Springer.

Wharton, S., Alai, M., & Myers, K. (2011). Meteorological observations for renewable energy applications at Site 300 (No. LLNL-TR-509672). Livermore, CA: Lawrence Livermore National Laboratory (LLNL). Retrieved from http://www.osti.gov/scitech/biblio/1035288

Wilde, M. (2012). The use of real-time off-site observations as a methodology for increasing forecast skill in prediction of large wind power ramps one or more hours ahead of their impact on a wind plant. (No. DOE/EE01388-F). WINData LLC. Retrieved from http://www.osti.gov/scitech/biblio/1062998

Wind rose plot. (2003). Natural Resources Conservation Service. Retrieved November 15, 2014, from http://www.wcc.nrcs.usda.gov/ftpref/downloads/climate/windrose/california/bakersfield/bakersfield_jun.gif

Wind roses. (2014). Iowa Environmental Mesonet. Retrieved November 15, 2014, from http://mesonet.agron.iastate.edu/onsite/windrose/climate/monthly/06/TSP_jun.png

Zhang, Y., Wang, J., & Wang, X. (2014). Review on probabilistic forecasting of wind power generation. Renewable & Sustainable Energy Reviews, 32, 255; 255-270; 270.

APPENDIX A

PERMISSION LETTER FOR SPRINGER CONTENT

Springer

PERMISSION LETTER

October 30, 2014

Springer reference

2006 Physical Approach to Short-Term Wind Power Prediction
Authors: Dr. Matthias Lange, Dr. Ulrich Focken

Material to be used: fig. 3.1
DOI 10.1007/3-540-31106-8
Print ISBN 978-3-540-25662-5
Online ISBN 978-3-540-31106-5

Your project

Requestor: Beth Magerman
Beth.Magerman@asu.edu
University: Arizona State University
Purpose: Dissertation/Thesis

With reference to your request to reuse material in which **Springer Science+Business Media** controls the copyright, our permission is granted free of charge under the following conditions:

Springer material

- represents original material which does not carry references to other sources (if material in question refers with a credit to another source, authorization from that source is required as well);
- requires full credit (Springer and the original publisher, book/journal title, chapter/article title, volume, year of publication, page, name(s) of author(s), original copyright notice) to the publication in which the material was originally published by adding: "With kind permission of Springer Science+Business Media";
- figures, illustrations, and tables may be altered minimally to serve your work. Any other abbreviations, additions, deletions and/or any other alterations shall be made only with prior written authorization of the author and/or Springer Science+Business Media;
- Springer does not supply original artwork or content.

This permission

- is non-exclusive;
- is valid for one-time use only for the purpose of defending your thesis limited to university-use only and with a maximum of 100 extra copies in paper. If the thesis is going to be published, permission needs to be reobtained.
- includes use in an electronic form, provided it is an author-created version of the thesis on his/her own website and his/her university's repository, including UMI (according to the definition on the Sherpa website: http://www.sherpa.ac.uk/romeo/);
- is subject to courtesy information to the author (address is given in the publication);
- is personal to you and may not be sublicensed, assigned, or transferred by you to any other person without Springer's written permission.